

Laser-induced surface magnetization in Floquet-Weyl semimetalsRunnan Zhang ¹, Ken-ichi Hino ^{2,3,*}, Nobuya Maeshima ³, Haruki Yogemura,¹ and Takeru Karikomi¹¹*Graduate School of Science and Technology, University of Tsukuba, Tsukuba, Ibaraki 305-8573, Japan*²*Institute of Pure and Applied Sciences, University of Tsukuba, Tsukuba, Ibaraki 305-8573, Japan*³*Center for Computational Sciences, University of Tsukuba, Tsukuba, Ibaraki 305-8577, Japan*

(Received 3 July 2023; revised 8 September 2023; accepted 29 September 2023; published 18 October 2023)

We investigate optically induced magnetization in Floquet-Weyl semimetals generated by irradiation of a circularly polarized continuous-wave laser from the group II-V narrow gap semiconductor Zn_3As_2 in a theoretical manner. Here, this trivial and nonmagnetic crystal is driven by the laser with a nearly resonant frequency with a band gap to generate two types of Floquet-Weyl semimetal phases composed of different spin states. These two phases host nontrivial two-dimensional surface states pinned to the respective pairs of the Weyl points. By numerically evaluating the laser-induced transient carrier dynamics, it is found that both spins are distributed in an uneven manner on the corresponding surface states due to significantly different excitation probabilities caused by the circularly polarized laser with the nearly resonant frequency. It is likely that such spin-polarized surface states produce surface magnetization and furthermore the inverse Faraday effect also contributes almost as much as the spin magnetization. To be more specific, excited carriers with high density of the order of 10^{21} cm^{-3} are generated by the laser with electric field strength of a few MV/cm to result in the surface magnetization that becomes asymptotically constant with respect to time, around 1 mT. The magnitude and the direction of it depend sharply on both the intensity and frequency of the driving laser, which would be detected by virtue of the magneto-optic Kerr effect.

DOI: [10.1103/PhysRevB.108.155308](https://doi.org/10.1103/PhysRevB.108.155308)**I. INTRODUCTION**

Weyl semimetals (WSMs) that belong to a class of topological semimetals (SMs) [1–15] have been extensively studied from the perspective of the nontrivial topology leading to many intriguing features of unusual electronic, magnetic, and optical properties. Low-energy excitation of WSMs is described by the Weyl equation characteristic of a linearly dispersive gapless band and well-defined chirality, where the Berry curvature shows a monopole at the resulting crossing point termed the Weyl node. The WSMs result in fundamental properties such as Fermi arc surface states, axion electrodynamics, and chiral anomaly (the Adler-Bell-Jackiw anomaly) proposed in particle physics [16–21]. Further, these exhibit a great number of novel transport properties [13,14], such as ultrahigh mobility [22], titanic magnetic resistance [22], anomalous Hall conductivity [4,23–27], and large negative magnetic resistance observed in magnetotransport attributed to the chiral anomaly [24,28–31]. The WSMs are created by breaking of either time reversal symmetry or spatial-inversion symmetry from Dirac SMs and nodal-line SMs that are different types of topological SMs [14,15]. In the WSMs with the time reversal symmetry breaking, there are a pair of Weyl nodes with opposite chirality, while, in those with the spatial-inversion symmetry breaking, the number of Weyl nodes is a multiple of four [2,14].

The introduction of an interaction of electron with a monochromatic continuous-wave laser with circular polarization also breaks the time reversal symmetry of the Dirac and nodal-line SMs to lead to a WSM state in nonequilibrium [32–39]. Due to the temporal periodicity of the Hamiltonian of concern, the Floquet theorem ensures the existence of a set of quasienergy bands (Floquet bands) associated with the WSM states, termed as Floquet WSM (FWSM) states. The physical properties of the FWSMs can be controlled by means of built-in laser parameters such as intensity, frequency, and polarization, giving rise to band modulation and topological phase transitions. The creation and optical control of Floquet states, termed as the Floquet engineering, provide a new avenue for the quantum control of topological materials [40–43]. In passing, the spatial inversion symmetry is also broken by the application of the monochromatic continuous-wave laser. However, the time-glide spatial inversion symmetry holds correct instead to realize the same invariance in the Hamiltonian as the spatial inversion symmetry [44,45].

In recent years, there has been a growing interest in the FWSMs for exploring new topological properties that cannot be realized in WSMs in equilibrium [46–61]. It is found that the drive of a three-dimensional Luttinger SM by an elliptically polarized light leads to the coexistence of WSM phases with double and single Weyl points, which can be tuned to be type I or type II [56], and the periodical driving of hybrid multi-WSM phases modulates the number of various isolated band touching points on demand by tuning system parameters [57]. Further, chirality switching of Weyl nodes is observed in a ferromagnetic Weyl semimetal excited by circularly

*hino@ims.tsukuba.ac.jp

polarized midinfrared light pulses, which accompanies the reversal of magnetization [60].

It has been reported very recently that two different spin-polarized FWSM phases are created at one time by irradiating on a trivial narrow gap semiconductor, Zn_3As_2 , an intense circularly polarized laser with frequency that is almost on resonant with the band gap [59]. This is due to the fact that an electric-dipole transition induced by this laser between valence and conduction bands with one spin state is dominant over that between bands with the other spin state. To be more specific, given the driving laser with a left-hand circular polarization (rotating in counterclockwise sense with time), the dipole coupling between the down-spin bands is much greater than that between the up-spin bands. Thus two types of Floquet bands with distinct energy structures are generated by the hybridization of valence and conduction bands with each spin state. In particular, the resulting up-spin Floquet band forms just a considerably smaller band gap than that of the down-spin Floquet band, similar to a nodal line SM with a band crossing in the shape of a closed ring. Furthermore, the associated surface states supported by these two Floquet bands also differ a lot from each other in energy structure. This finding is much contrasted with properties of the FWSMs induced by a circularly polarized laser with an off-resonant frequency [32,35,62], in which a high-frequency approximation based on the Floquet-Magnus expansion [63–67] is warranted.

This paper is aimed at examining the possibility of the manifestation of transient magnetization attributed to the above-stated difference of the dipole couplings in the FWSM created by the on-resonant drive. It is stressed that real carrier excitations caused by such transient quantum dynamics play crucial roles of the magnetization, differing from the off-resonant drive just causing virtual excitations. Due to the application of the intense laser with a peak electric field of the order of 1 MV/cm, down-spin electrons are considered to be more dominantly excited than up-spin electrons, resulting in the imbalance of spin distributions between the respective Floquet bands. It is likely that conspicuous surface magnetization arises from such imbalance of spin distributions, namely, the surface spin polarization, where the associated bulk magnetization is also induced, but however actually neglected compared with the surface one, as shown later (Sec. III). Furthermore, it is considered that the inverse Faraday effect (IFE) contributes to the surface magnetization to some extent in addition to the above spin magnetization. The IFE is given rise to by the laser with circular polarization and the orbital magnetization is generated, which remains constant in time [50–53,68–81]. Differing from the conventional IFE arising from the second-order optical process with respect to the electric field of the laser, it is expected that the higher order terms come into play for the orbital magnetization concerned here due to the application of the intense laser. In passing, it is remarked that the IFE on WSMs, differing from the present FWSMs, has been studied recently to exhibit frequency-independent magnetization mechanisms [50,51].

The remainder of this paper is organized as follows. Section II describes the theoretical framework, Sec. III presents the results and discussion, and Sec. IV presents the conclusion. Further, three Appendixes are included. Hereafter,

the atomic units (a.u.) are used throughout, unless otherwise stated.

II. THEORY

In this section, one begins with the construction of the Floquet Hamiltonian in Sec. II A, followed by the description of the density matrices for the laser-induced dynamics of concern in Sec. II B and of the laser-induced magnetization in Sec. II C.

A. Floquet Hamiltonian

The crystal adopted here is the group II-V narrow gap semiconductor, Zn_3As_2 , with the C_4 -rotational symmetry along the $\Gamma - Z$ axis in the Brillouin zone (BZ). This structure is similar to that of Cd_3As_2 , though the band of the latter is inverted to result in a Dirac SM [82–86]. Here, one employs the structure of $\alpha'\text{Zn}_3\text{As}_2$ with a tetragonal structure $P4_2/nbc$ [87] among many equilibrium phases of Zn_3As_2 depending on pressure and temperature.

An effective electronic Hamiltonian of this crystal is constructed based on the Kane model [4,59] in view of the low-energy electronic properties mostly determined by the conduction band composed of Zn 4s orbitals and the valence band composed of As 4p orbitals. Thus the following four states are considered as conduction s states $|\Gamma_6, J_z = \pm 1/2\rangle$ and heavy-hole p states $|\Gamma_7, J_z = \pm 3/2\rangle$, where J_z represents the z component of the total angular momentum quantum number at the Γ point with a three-dimensional (3D) Bloch momentum $\mathbf{k} = (k_x, k_y, k_z)$ being equal to zero. Here, light-hole states and split-off states are disregarded because of relatively large energy separation from these four states at the Γ point. The effective Hamiltonian is given by the 4×4 matrix [88,89]:

$$\mathcal{H}(\mathbf{k}) = \sum_{j=3}^5 D_j(\mathbf{k})\gamma_j, \quad (1)$$

where γ_j 's represent the four-dimensional Dirac matrices for the Clifford algebra ensuring the anticommutation relation, $\{\gamma_j, \gamma_{j'}\} = 2\delta_{jj'}$, defined by $\gamma_1 = \tau_x \otimes \sigma_x$, $\gamma_2 = \tau_x \otimes \sigma_y$, $\gamma_3 = \tau_x \otimes \sigma_z$, $\gamma_4 = \tau_z \otimes I_2$, and $\gamma_5 = \tau_y \otimes I_2$; I_2 represents the 2×2 unit matrix, and τ_l and σ_l with $l = x, y, z$ represent the Pauli matrices for orbital and spin degrees of freedom, respectively. According to the above definition of γ_j 's, it is understood that the states of $|\Gamma_6, J_z = 1/2\rangle$, $|\Gamma_7, J_z = 3/2\rangle$, $|\Gamma_6, J_z = -1/2\rangle$, and $|\Gamma_7, J_z = -3/2\rangle$ are labeled as 1, 2, 3, and 4, respectively, for the matrix elements of $\mathcal{H}(\mathbf{k})$, namely, $\{\mathcal{H}_{mn}(\mathbf{k})\}$ with $m, n = 1-4$. Moreover, $D_j(\mathbf{k})$'s are given by

$$\begin{aligned} D_3(\mathbf{k}) &= t_{sp} \sin(k_x d_x), \\ D_4(\mathbf{k}) &= \Delta_g - 2 \sum_{l=x,y,z} t^l \{1 - \cos(k_l d_l)\}, \\ D_5(\mathbf{k}) &= t_{sp} \sin(k_y d_y). \end{aligned} \quad (2)$$

Here, t^l represents a hopping matrix between identical bands in the l direction with $l = x, y, z$, where $t^l < 0$ and $t^x = t^y$, and t_{sp} represents a hopping matrix between different bands

due to a spin-orbit coupling. Further, d_l represents a lattice constant in the l direction and the band gap at the Γ -point E_g is given by the difference of the energy of the conduction band at Γ_6 from that of the valence band at Γ_7 with $\Delta_g = E_g/2$.

An interaction of electron with light is introduced into $\mathcal{H}(\mathbf{k})$ by replacing \mathbf{k} by $\mathbf{K}(t) = \mathbf{k} + \mathbf{A}(t)$, followed by adding to $\mathcal{H}(\mathbf{K}(t))$ an interband electric-dipole interaction represented by $\mathcal{H}'(t)$. Here, $\mathbf{A}(t)$ represents a vector potential of the laser at time t , given by

$$\mathbf{A}(t) = \left(-\frac{F_x}{\omega} \sin \omega t, \frac{F_y}{\omega} \cos \omega t, 0 \right), \quad (3)$$

with ω as frequency and F_x and F_y as constants, and in view of $\mathbf{F}(t) = -\dot{\mathbf{A}}(t)$, the associated electric field becomes

$$\mathbf{F}(t) = (F_x \cos \omega t, F_y \sin \omega t, 0). \quad (4)$$

The laser is linearly polarized in the x direction when $F_x \neq 0$ and $F_y = 0$, while being left-hand circularly polarized in the $x - y$ plane when F_x is set equal to F_y , namely, $F_c \equiv F_x = F_y$. The time-dependent effective Hamiltonian of the driven semiconductor is thus read as

$$H_F(\mathbf{k}, t) = \mathcal{H}(\mathbf{K}(t)) + \mathcal{H}'(t), \quad (5)$$

where

$$\mathcal{H}(\mathbf{K}(t)) = \sum_{j=3}^5 D_j(\mathbf{K}(t)) \gamma_j. \quad (6)$$

The interband electric-dipole interaction is provided as [59]

$$\mathcal{H}'(t) = (\Omega_x \sin \omega t) \tau_x \otimes I_2 + (\Omega_x \cos \omega t) \tau_y \otimes \sigma_z, \quad (7)$$

where $\Omega_x = F_x P / \sqrt{2}$ and $\Omega_y = F_y P / \sqrt{2}$. Here, P is a dipole matrix element given by $P = \langle S|x|X \rangle = \langle S|y|Y \rangle$, where x and y represent the x and y components of electron position \mathbf{r} , respectively, and the states of $|\Gamma_6, J_z = \pm 1/2 \rangle$ and $|\Gamma_7, J_z = \pm 3/2 \rangle$ are represented by $|\Gamma_6, J_z = \pm 1/2 \rangle = i|S \rangle$ and $|\Gamma_7, J_z = \pm 3/2 \rangle = \pm(1/\sqrt{2})|X \pm iY \rangle$, respectively, in terms of s , p_x , and p_y states denoted as $|S \rangle$, $|X \rangle$, and $|Y \rangle$, respectively.

Obviously, this Hamiltonian ensures the temporal periodicity, $H_F(\mathbf{k}, t + T) = H_F(\mathbf{k}, t)$ with $T = 2\pi/\omega$, and the system of concern follows the Floquet theorem [90]. Thus the present time-dependent problem ends up with the following Floquet eigenvalue problem as

$$L_F(\mathbf{k}, t) \phi_{k\alpha}(t) = E_\alpha(\mathbf{k}) \phi_{k\alpha}(t), \quad (8)$$

where $L_F(\mathbf{k}, t)$ is the Floquet Hamiltonian defined as

$$L_F(\mathbf{k}, t) = H_F(\mathbf{k}, t) - iI \frac{\partial}{\partial t}, \quad (9)$$

with I the 4×4 unit matrix, $E_\alpha(\mathbf{k})$ representing an eigenvalue showing the α th Floquet energy, and $\phi_{k\alpha}(t)$ representing the associated eigenvector ensuring the temporal periodicity, $\phi_{k\alpha}(t + T) = \phi_{k\alpha}(t)$. Hereafter, it is understood that the photon sideband α is represented as $\alpha_0(N_\alpha)$, where $\alpha_0[\equiv \alpha_0(0)]$ and N_α stand for a parent band and the number of the sideband, respectively. Further, $\alpha(N) \equiv \alpha_0(N_\alpha + N)$ and $E_{\alpha(N)}(\mathbf{k}) \equiv E_\alpha(\mathbf{k}) + N\omega = E_{\alpha_0}(\mathbf{k}) + (N_\alpha + N)\omega$, with N being an integer.

For the purpose of later convenience, the wave function $\phi_{k\alpha}(t)$ is represented in view of the above periodicity as

$$\phi_{k\alpha}(t) = \sum_{\mu} \chi_{\mu} \varphi_{\mu, k\alpha}(t), \quad (10)$$

where χ_{μ} represents the μ th state corresponding to $|\Gamma_6, J_z = \pm 1/2 \rangle$ and $|\Gamma_7, J_z = \pm 3/2 \rangle$, and the periodic function $\varphi_{\mu, k\alpha}(t)$ is given in terms of the Fourier expansion as

$$\varphi_{\mu, k\alpha}(t) = \sum_n e^{in\omega t} C_{\mu n, k\alpha}. \quad (11)$$

Thus Eq. (8) is recast into

$$\sum_{\nu} L_{F\nu\nu}(\mathbf{k}, t) \varphi_{\nu, k\alpha}(t) = E_\alpha(\mathbf{k}) \varphi_{\mu, k\alpha}(t), \quad (12)$$

where

$$L_{F\nu\nu}(\mathbf{k}, t) = H_{F\nu\nu}(\mathbf{k}, t) - \delta_{\mu\nu} i \frac{d}{dt} \quad (13)$$

and

$$\sum_{\nu\nu'} L_{F\nu\nu'}(\mathbf{k}) C_{\nu\nu', k\alpha} = E_\alpha(\mathbf{k}) C_{\mu n, k\alpha}, \quad (14)$$

where

$$L_{F\nu\nu'}(\mathbf{k}) = \frac{1}{T} \int_0^T dt e^{-in\omega t} L_{F\nu\nu}(\mathbf{k}, t) e^{in'\omega t}. \quad (15)$$

B. Density matrices

In the actual physical system, the intense monochromatic laser with circular polarization is exerted on the crystal at a certain time, for example, at $t = 0$, leading to high-density carrier excitation followed by dephasing and relaxation. The detail of this transient dynamics with concomitant physical phenomena can be examined by tracking the alteration of the associated density matrices in time. The one-electron Hamiltonian representing the dynamics is given by

$$H(\mathbf{k}, t) = \mathcal{H}(\mathbf{k}) + V(\mathbf{k}, t), \quad (16)$$

where

$$V(\mathbf{k}, t) \equiv [H_F(\mathbf{k}, t) - \mathcal{H}(\mathbf{k})] \theta(t) \quad (17)$$

under the tacit assumption that temporal width of the applied laser pulse is sufficiently long. Obviously, $H(\mathbf{k}, t + T) \neq H(\mathbf{k}, t)$, since $H(\mathbf{k}, t) = \mathcal{H}(\mathbf{k})$ for $t < 0$ and $H(\mathbf{k}, t) = H_F(\mathbf{k}, t)$ for $t > 0$. Employing Eq. (16), the total Hamiltonian represented by $\hat{H}(t)$ is read as

$$\hat{H}(t) = \sum_{k\mu\nu} H_{\mu\nu}(\mathbf{k}, t) \hat{a}_{k\mu}^\dagger(t) \hat{a}_{k\nu}(t), \quad (18)$$

where $\hat{a}_{k\mu}^\dagger(t)$ and $\hat{a}_{k\mu}(t)$ represent creation and annihilation operators of state μ at \mathbf{k} in the Heisenberg representation, respectively, and electron-electron interactions are neglected for the sake of simplicity. Furthermore, for a given \mathbf{k} , the field operator of the system is provided by

$$\hat{\psi}_{\mathbf{k}}(t) = \sum_{\mu} \chi_{\mu} \hat{a}_{k\mu}(t). \quad (19)$$

The time evolution of operator $\hat{a}_{k\lambda}(t)$ follows the Heisenberg equation of

$$\begin{aligned} i\frac{d\hat{a}_{k\lambda}(t)}{dt} &= [\hat{a}_{k\lambda}(t), \hat{H}(t)] \\ &= \sum_{\nu} H_{\lambda\nu}(\mathbf{k}, t)\hat{a}_{k\nu}(t), \end{aligned} \quad (20)$$

where the equal-time anticommutation relation $\{\hat{a}_{k\mu}(t), \hat{a}_{k'\nu}^{\dagger}(t)\} = \delta_{\mu\nu}\delta_{kk'}$ is employed. Hence it is shown that a reduced density matrix, defined by

$$\rho_{k\mu\nu}(t) = \langle \hat{a}_{k\mu}^{\dagger}(t)\hat{a}_{k\nu}(t) \rangle_g, \quad (21)$$

ensures the equation of motion given by

$$\begin{aligned} i\frac{d\rho_{k\mu\nu}(t)}{dt} &= \langle [\hat{a}_{k\mu}^{\dagger}(t)\hat{a}_{k\nu}(t), \hat{H}(t)] \rangle_g \\ &= \sum_{\lambda} [-H_{\mu\lambda}^*(\mathbf{k}, t)\rho_{k\lambda\nu}(t) + H_{\lambda\nu}^*(\mathbf{k}, t)\rho_{k\mu\lambda}(t)]. \end{aligned} \quad (22)$$

Hereafter, the reduced density matrix Eq. (21) is simply termed as a density matrix. $\langle \hat{X} \rangle_g$ represents a ground state expectation value of operator \hat{X} . In addition, the contributions of phenomenological damping have to be incorporated with Eq. (22), as is taken account of later.

Now, the operator $\hat{b}_{k\alpha}^{\dagger}(t)$ is defined as

$$\hat{b}_{k\alpha}^{\dagger}(t) = \sum_{\mu} \hat{a}_{k\mu}^{\dagger}(t)\varphi_{\mu,k\alpha}(t)\theta(t), \quad (23)$$

which brings the operator $\hat{a}_{k\mu}^{\dagger}(t)$ to

$$\hat{a}_{k\mu}^{\dagger}(t) = \sum_{\alpha} \hat{b}_{k\alpha}^{\dagger}(t)C_{\mu 0, k\alpha}^*, \quad (24)$$

as is shown in Eq. (A16). Hence the field operator of Eq. (19) is rewritten as

$$\begin{aligned} \hat{\psi}_{\mathbf{k}}(t) &= \sum_{\mu\alpha} \chi_{\mu} C_{\mu 0, k\alpha} \hat{b}_{k\alpha}(t) \\ &= \sum_{\alpha_0} \phi_{k\alpha_0}(t)\hat{b}_{k\alpha_0}(t), \end{aligned} \quad (25)$$

where Eqs. (10), (A12), and (A13) are employed. The equal-time anticommutation between $\hat{b}_{k\alpha}(t)$ and $\hat{b}_{k'\alpha'}^{\dagger}(t)$ is evaluated in view of Eq. (11) as

$$\begin{aligned} \{\hat{b}_{k\alpha}(t), \hat{b}_{k'\alpha'}^{\dagger}(t)\} &= \delta_{kk'} \sum_{\mu} \varphi_{\mu,k\alpha}(t)\varphi_{\mu,k'\alpha'}^*(t) \\ &= \delta_{kk'} \sum_{\mu n \Delta n} e^{i\Delta n \omega t} C_{\mu n, k\alpha} C_{\mu n, k'\alpha'}^*(\Delta n) \\ &= \delta_{kk'} \sum_{\Delta n} e^{i\Delta n \omega t} \delta_{\alpha_0 \alpha'_0} \delta_{N_{\alpha}, (N_{\alpha'} + \Delta n)} \\ &= \delta_{kk'} e^{i(N_{\alpha} - N_{\alpha'})\omega t} \delta_{\alpha_0 \alpha'_0}. \end{aligned} \quad (26)$$

Thus one obtains the anticommutation relation that

$$\{\hat{b}_{k\alpha_0}(t), \hat{b}_{k'\alpha'_0}^{\dagger}(t)\} = \delta_{kk'} \delta_{\alpha_0 \alpha'_0}, \quad (27)$$

which implies that $\hat{b}_{k\alpha_0}(t)$ and $\hat{b}_{k'\alpha'_0}^{\dagger}(t)$ play the role of fermion operators.

Next, the equation of motion of $\hat{b}_{k\alpha_0}(t)$ is derived. In view of Eq. (20) with Eqs. (23) and (24),

$$\begin{aligned} i\frac{d\hat{b}_{k\alpha_0}(t)}{dt} &= \sum_{\nu} \left(i\frac{d\hat{a}_{k\nu}(t)}{dt} \varphi_{\nu, k\alpha_0}^*(t) + \hat{a}_{k\nu}(t) i\frac{d\varphi_{\nu, k\alpha_0}^*(t)}{dt} \right) \\ &\quad + i\hat{b}_{k\alpha_0}(0)\delta(t) \\ &= [\hat{b}_{k\alpha_0}(t), \hat{H}(t)] + \sum_{\nu} \hat{a}_{k\nu}(t) i\frac{d\varphi_{\nu, k\alpha_0}^*(t)}{dt} \\ &\quad + i\hat{b}_{k\alpha_0}(0)\delta(t). \end{aligned} \quad (28)$$

On the other hand, defining another Hamiltonian as

$$\hat{L}(t) = \sum_{k\alpha_0} E_{\alpha_0}(\mathbf{k})\hat{b}_{k\alpha_0}^{\dagger}(t)\hat{b}_{k\alpha_0}(t), \quad (29)$$

and employing Eq. (23), this is cast into

$$\begin{aligned} \hat{L}(t) &= \sum_{k\alpha_0 n \mu \nu} E_{\alpha_0}(\mathbf{k})\varphi_{\mu, k\alpha_0}(t) e^{-in\omega t} C_{\nu n, k\alpha_0}^* \hat{a}_{k\mu}^{\dagger}(t)\hat{a}_{k\nu}(t) \\ &= \sum_{k\alpha_0 n \mu \nu} [E_{\alpha_0(-n)}(\mathbf{k}) + n\omega] \varphi_{\mu, k\alpha_0(-n)}(t) \\ &\quad \times C_{\nu 0, k\alpha_0(-n)}^* \hat{a}_{k\mu}^{\dagger}(t)\hat{a}_{k\nu}(t) \\ &= \sum_{k\mu\nu} H_{\mu\nu}(\mathbf{k}, t)\hat{a}_{k\mu}^{\dagger}(t)\hat{a}_{k\nu}(t) \\ &\quad + \sum_{k\alpha_0 n \nu} n\omega C_{\nu 0, k\alpha_0(-n)}^* e^{-in\omega t} \hat{b}_{k\alpha_0}^{\dagger}(t)\hat{a}_{k\nu}(t) \\ &= \hat{H}(t) + \sum_{k\alpha_0 \nu} \hat{b}_{k\alpha_0}^{\dagger}(t)\hat{a}_{k\nu}(t) i\frac{d\varphi_{\nu, k\alpha_0}^*(t)}{dt}, \end{aligned} \quad (30)$$

where Eqs. (11), (A10), (A14), (A21), and (24) are employed. Putting the above result into the first term in the second equality of Eq. (28) leads to

$$\begin{aligned} i\frac{d\hat{b}_{k\alpha_0}(t)}{dt} &= [\hat{b}_{k\alpha_0}(t), \hat{L}(t)] \\ &\quad - \left[\hat{b}_{k\alpha_0}(t), \sum_{k\alpha'_0 \nu} \hat{b}_{k\alpha'_0}^{\dagger}(t)\hat{a}_{k\nu}(t) i\frac{d\varphi_{\nu, k\alpha'_0}^*(t)}{dt} \right] \\ &\quad + \sum_{k\nu} \hat{a}_{k\nu}(t) i\frac{d\varphi_{\nu, k\alpha_0}^*(t)}{dt} + i\hat{b}_{k\alpha_0}(0)\delta(t) \\ &= [\hat{b}_{k\alpha_0}(t), \hat{L}(t)] + i\hat{b}_{k\alpha_0}(0)\delta(t), \end{aligned} \quad (31)$$

where Eq. (27) is employed. This becomes of the form of

$$i\frac{d\hat{b}_{k\alpha_0}(t)}{dt} = E_{\alpha_0}(\mathbf{k})\hat{b}_{k\alpha_0}(t) + i\hat{b}_{k\alpha_0}(0)\delta(t) \quad (32)$$

and the solution of it is given by

$$\hat{b}_{k\alpha_0}(t) = \hat{b}_{k\alpha_0}(0)e^{-iE_{\alpha_0}(\mathbf{k})t}\theta(t). \quad (33)$$

Applying Eq. (A14), eventually, one obtains

$$\hat{b}_{k\alpha}(t) = \hat{b}_{k\alpha}(0)e^{-iE_{\alpha}(\mathbf{k})t}\theta(t), \quad (34)$$

with $\alpha = \alpha_0(N_\alpha)$ and $\hat{b}_{k\alpha_0}(0) = \hat{b}_{k\alpha}(0)$. Further, it should be noted that the equation of motion of $\hat{b}_{k\alpha_0}(t)$ given by Eq. (31) for $t > 0$ corresponds to the Heisenberg equation with the effective Hamiltonian $\hat{L}(t)$. This implies that the Floquet state ($k\alpha_0$) is considered as a fermionic quasiparticle, ensuring the anticommutation relation Eq. (27).

According to the above results, the density matrix of Eq. (21) is recast into

$$\rho_{k\mu\nu}(t) = \sum_{\alpha\alpha'} \bar{\rho}_{k\alpha\alpha'}(t) C_{\mu 0, k\alpha}^* C_{\nu 0, k\alpha'}, \quad (35)$$

where a density matrix of the quasiparticle is introduced as

$$\begin{aligned} \bar{\rho}_{k\alpha\alpha'}(t) &= \langle \hat{b}_{k\alpha}^\dagger(t) \hat{b}_{k\alpha'}(t) \rangle_g \\ &= \bar{\rho}_{k\alpha\alpha'}(0) e^{i[E_\alpha(k) - E_{\alpha'}(k)]t} \theta(t). \end{aligned} \quad (36)$$

On the other hand, by employing Eq. (23), one obtains

$$\bar{\rho}_{k\alpha\alpha'}(0) = \sum_{\mu\nu\nu'} \rho_{k\mu\nu}(0) C_{\mu\nu, k\alpha} C_{\nu\nu', k\alpha'}^*, \quad (37)$$

providing the initial conditions of the quasiparticle states in Eq. (36) that are represented in terms of initial values of the original density matrix $\rho_{k\mu\nu}(0)$. Here, $\rho_{k\mu\nu}(0) = \delta_{\mu\nu} \delta_{\mu\nu}$, with ν a band index corresponding to valence bands of states $|\Gamma_7, J_z = \pm 3/2\rangle$.

Moreover, by incorporating the phenomenological damping terms with the equation of motion of the density matrices $\rho_{k\mu\nu}(t)$ of Eq. (22), $\bar{\rho}_{k\alpha\alpha'}(t)$ for $t > 0$ is modified to

$$\bar{\rho}_{k\alpha\alpha}(t) = \bar{\rho}_{k\alpha\alpha}(0) e^{-t/T_1} + \bar{\rho}_{k\alpha\alpha}(t_{eq}) (1 - e^{-t/T_1}) \quad (38)$$

for $\alpha = \alpha'$ and

$$\bar{\rho}_{k\alpha\alpha'}(t) = \bar{\rho}_{k\alpha\alpha'}(0) e^{i[E_\alpha(k) - E_{\alpha'}(k)]t - t/T_2} \quad (39)$$

for $\alpha \neq \alpha'$ (see Supplemental Material [91]). Here, T_1 and T_2 represent longitudinal and transverse relaxation times, respectively, and t_{eq} represents quasiequilibrium time, where $t_{eq} \gg T_1$. Apparently, these expressions are in agreement with Eq. (36) in the limit of $T_1, T_2 \rightarrow \infty$.

C. Laser-induced magnetization

Here, one presents an exact quantum-mechanical description of an optically induced magnetization imparted by an intense laser with circular polarization within the electric dipole approximation. This provides a materials-specific framework for the calculation of the optomagnetic polarization in a nonperturbative manner with respect to laser intensity, not limited to model systems.

1. Solenoid current density and magnetization

One begins with the following Hamiltonian as

$$h(\mathbf{r}, t) = h^0(\mathbf{r}) + V(\mathbf{r}, t), \quad (40)$$

where $h^0(\mathbf{r})$ represents a one-electron material Hamiltonian, given by

$$h^0(\mathbf{r}, t) = -\frac{\nabla^2}{2} + v(\mathbf{r}) + v_{so}(\mathbf{r}), \quad (41)$$

with $v(\mathbf{r})$ and $v_{so}(\mathbf{r})$ as a periodic potential of crystal and a spin-orbit interaction, respectively, and $V(\mathbf{r}, t)$ represents the electric dipole interaction with the laser, given by

$$V(\mathbf{r}, t) = \mathbf{F}(t) \cdot \mathbf{r}. \quad (42)$$

Here, a field operator $\hat{\Psi}(\mathbf{r}, t)$ is defined so as to ensure the equation of motion

$$i \frac{\partial \hat{\Psi}(\mathbf{r}, t)}{\partial t} = h(\mathbf{r}, t) \hat{\Psi}(\mathbf{r}, t), \quad (43)$$

with the equal-time anticommutation relation

$$\{\hat{\Psi}(\mathbf{r}, t), \hat{\Psi}^\dagger(\mathbf{r}', t)\} = \delta(\mathbf{r} - \mathbf{r}'). \quad (44)$$

Accordingly, it is readily seen that the charge density of electron represented by

$$\rho(\mathbf{r}, t) = -\langle \hat{\Psi}^\dagger(\mathbf{r}, t) \hat{\Psi}(\mathbf{r}, t) \rangle_g \quad (45)$$

follows the equation of continuity,

$$\frac{\partial \rho(\mathbf{r}, t)}{\partial t} + \nabla \cdot \mathbf{j}(\mathbf{r}, t) = 0, \quad (46)$$

where $\mathbf{j}(\mathbf{r}, t)$ represents the charge current density of electron, given by

$$\mathbf{j}(\mathbf{r}, t) = -\text{Re} \langle -i \hat{\Psi}^\dagger(\mathbf{r}, t) \nabla \hat{\Psi}(\mathbf{r}, t) \rangle_g. \quad (47)$$

On the other hand, Ampère's circuital law is read as

$$\nabla \times \frac{\mathbf{B}(\mathbf{r}, t)}{\mu_0} = \mathbf{j}_{\text{tot}}(\mathbf{r}, t) + \frac{\partial \varepsilon_0 \mathbf{E}(\mathbf{r}, t)}{\partial t}, \quad (48)$$

where $\mathbf{E}(\mathbf{r}, t)$ and $\mathbf{B}(\mathbf{r}, t)$ represent an electric field and a magnetic flux density, respectively, with ε_0 and μ_0 the permittivity of vacuum and the permeability of vacuum, respectively. The total current density $\mathbf{j}_{\text{tot}}(\mathbf{r}, t)$ is provided by the sum of the free current density $\mathbf{j}(\mathbf{r}, t)$ and bound current densities as

$$\mathbf{j}_{\text{tot}}(\mathbf{r}, t) = \mathbf{j}(\mathbf{r}, t) + \mathbf{j}_m(\mathbf{r}, t) + \mathbf{j}_p(\mathbf{r}, t), \quad (49)$$

where $\mathbf{j}_m(\mathbf{r}, t)$ and $\mathbf{j}_p(\mathbf{r}, t)$ represent the bound currents ascribable to magnetization $\mathbf{M}(\mathbf{r}, t)$ and polarization $\mathbf{P}(\mathbf{r}, t)$ given by

$$\mathbf{j}_m(\mathbf{r}, t) = \nabla \times \mathbf{M}(\mathbf{r}, t) \quad (50)$$

and

$$\mathbf{j}_p(\mathbf{r}, t) = \frac{\partial \mathbf{P}(\mathbf{r}, t)}{\partial t}, \quad (51)$$

respectively. Since the polarization vector is read as

$$\mathbf{P}(\mathbf{r}, t) = -\langle \hat{\Psi}^\dagger(\mathbf{r}, t) \mathbf{r} \hat{\Psi}(\mathbf{r}, t) \rangle_g = \mathbf{r} \rho(\mathbf{r}, t), \quad (52)$$

the bound current density induced by this is rewritten as

$$\mathbf{j}_p(\mathbf{r}, t) = \mathbf{r} \frac{\partial \rho(\mathbf{r}, t)}{\partial t} = -\mathbf{r} \nabla \cdot \mathbf{j}(\mathbf{r}, t), \quad (53)$$

due to Eq. (46).

Employing the following formula [72]:

$$\mathbf{A} \nabla \cdot \mathbf{B} - \mathbf{B} \nabla \cdot \mathbf{A} = \nabla \times (\mathbf{A} \times \mathbf{B}) + \mathbf{A} \cdot \nabla \mathbf{B} - \mathbf{B} \cdot \nabla \mathbf{A}, \quad (54)$$

with $\mathbf{A} = -\mathbf{r}$ and $\mathbf{B} = \mathbf{j}(\mathbf{r}, t)$, Eq. (53) becomes

$$\begin{aligned} \mathbf{j}_p(\mathbf{r}, t) &= -\nabla \times [\mathbf{r} \times \mathbf{j}(\mathbf{r}, t)] - \mathbf{r} \cdot \nabla \mathbf{j}(\mathbf{r}, t) \\ &\quad - 2\mathbf{j}(\mathbf{r}, t). \end{aligned} \quad (55)$$

This brings the free current density to be of the form

$$\mathbf{j}(\mathbf{r}, t) = -\frac{1}{2}\{\nabla \times [\mathbf{r} \times \mathbf{j}(\mathbf{r}, t)] + \mathbf{r} \cdot \nabla \mathbf{j}(\mathbf{r}, t) - \mathbf{r} \nabla \cdot \mathbf{j}(\mathbf{r}, t)\}. \quad (56)$$

Therefore, the total current density becomes

$$\begin{aligned} \mathbf{j}_{\text{tot}}(\mathbf{r}, t) &= \mathbf{j}(\mathbf{r}, t) + \nabla \times \mathbf{M}(\mathbf{r}, t) - \mathbf{r} \nabla \cdot \mathbf{j}(\mathbf{r}, t) \\ &= \nabla \times \{\mathbf{M}(\mathbf{r}, t) - \frac{1}{2} \mathbf{r} \times \mathbf{j}(\mathbf{r}, t)\} \\ &\quad - \frac{1}{2} \{\mathbf{r} \cdot \nabla \mathbf{j}(\mathbf{r}, t) + \mathbf{r} \nabla \cdot \mathbf{j}(\mathbf{r}, t)\}. \end{aligned} \quad (57)$$

It is obvious that the first term in the last equality implies the solenoid current density $\mathbf{j}^{(\text{sol})}(\mathbf{r}, t)$ imparted by $\mathbf{j}_{\text{tot}}(\mathbf{r}, t)$. This gives rise to the magnetization given by

$$\mathbf{M}^{(\text{sol})}(\mathbf{r}, t) = \mathbf{M}(\mathbf{r}, t) - \frac{1}{2} \mathbf{r} \times \mathbf{j}(\mathbf{r}, t). \quad (58)$$

Here, the first term originates simply from spins of electrons and the other is ascribable to the polarization-induced magnetization.

The first term of Eq. (58) is expressed as

$$\mathbf{M}(\mathbf{r}, t) = \mu_B g_e \langle \hat{\Psi}^\dagger(\mathbf{r}, t) \mathbf{s} \hat{\Psi}(\mathbf{r}, t) \rangle_g, \quad (59)$$

with the spin angular momentum operator as $\mathbf{s} = \boldsymbol{\sigma}/2$, where Bohr magneton μ_B is introduced, namely, $\mu_B = 1/2$, and g_e represents the gyromagnetic ratio of electron spin. Moreover, the second term is given by

$$\mathbf{M}^{(2)}(\mathbf{r}, t) = \mu_B \text{Re}[\langle \hat{\Psi}^\dagger(\mathbf{r}, t) \mathbf{l} \hat{\Psi}(\mathbf{r}, t) \rangle_g]. \quad (60)$$

Here, this term ascribable to \mathbf{l} shows the contribution of the orbital magnetization caused by an elliptic trajectory of electron under the circularly polarized light field. The effect of magnetization thus induced is termed as the IFE as mentioned in Sec. I, which is understood as a second-order optical process caused exclusively by the irradiation of circularly polarized light. The above procedure of extracting the contribution of the orbital magnetization from $\mathbf{j}^{(\text{sol})}(\mathbf{r}, t)$ is also adopted in the perturbative manner in Ref. [72]. The obtained expression of IFE in terms of \mathbf{l} is identical with that introduced in Ref. [81], however, without a quantum-mechanical derivation. As shown right below, in fact, the term of \mathbf{l} is altered by the choice of a gauge factor incorporated in $\hat{\Psi}(\mathbf{r}, t)$ as an additional phase. Equation (60) is applicable to calculations of the optomagnetic polarization of any material induced by a circularly polarized laser with any laser intensity regardless of temporal width—ranging from an ultrashort pulse to a continuous wave laser. To be more specific, this is evaluated in terms of transient density matrices subject to nonequilibrium quantum dynamics, as shown below, differing from most theories of IFE just providing a stationary part of induced magnetization at an asymptotic limit [68,72–80].

In passing, as regards the second term of Eq. (57), it is shown that

$$\nabla \cdot \mathbf{j}_{\text{tot}}(\mathbf{r}, t) = -\frac{1}{2} \nabla \cdot \{\mathbf{r} \cdot \nabla \mathbf{j}(\mathbf{r}, t) + \mathbf{r} \nabla \cdot \mathbf{j}(\mathbf{r}, t)\}, \quad (61)$$

while, owing to Gauss' law, Eq. (48) becomes

$$\begin{aligned} 0 &= \nabla \cdot \mathbf{j}_{\text{tot}}(\mathbf{r}, t) + \frac{\partial \varepsilon_0 \nabla \cdot \mathbf{E}(\mathbf{r}, t)}{\partial t} \\ &= \nabla \cdot \mathbf{j}_{\text{tot}}(\mathbf{r}, t) + \frac{\partial \rho_{\text{tot}}(\mathbf{r}, t)}{\partial t}, \end{aligned} \quad (62)$$

where $\rho_{\text{tot}}(\mathbf{r}, t)$ represents the total charge density defined by the sum of $\rho(\mathbf{r}, t)$ and the polarized charge $\rho_p(\mathbf{r}, t) = -\nabla \cdot \mathbf{P}(\mathbf{r}, t)$, that is,

$$\rho_{\text{tot}}(\mathbf{r}, t) = \rho(\mathbf{r}, t) + \rho_p(\mathbf{r}, t). \quad (63)$$

Hence Eq. (61) is nothing but the equation of continuity for the total charge density and current density, and the right side of Eq. (61) is identical with $-\partial \rho_{\text{tot}}(\mathbf{r}, t)/\partial t$.

2. Gauge transformation

Below, we aim to represent Eqs. (59) and (60) in terms of the density matrix of Eq. (21) by taking an appropriate gauge transformation on $\hat{\Psi}(\mathbf{r}, t)$. Hereafter, a function $f(\mathbf{r})$ and an operator $\hat{\xi}(\mathbf{r})$ are represented as $\langle \mathbf{r} | f \rangle$ and $\langle \mathbf{r} | \hat{\xi} \rangle$, respectively, in terms of the Dirac notation, if necessary. Accordingly, Eq. (40) is rewritten as

$$h(\mathbf{r}, t) = \sum_{\mu, \mathbf{R}, \mu', \mathbf{R}'} \langle \mathbf{r} | \mu \mathbf{R} \rangle h_{\mu \mathbf{R}, \mu' \mathbf{R}'}(t) \langle \mu' \mathbf{R}' | \mathbf{r} \rangle \quad (64)$$

in terms of a set of Wannier states $\{|\mu \mathbf{R}\rangle\}$ with μ and \mathbf{R} a band index and a site vector of the crystal. Here,

$$\begin{aligned} h_{\mu \mathbf{R}, \mu' \mathbf{R}'}(t) &= \langle \mu \mathbf{R} | h^0 | \mu' \mathbf{R}' \rangle + \langle \mu \mathbf{R} | V | \mu' \mathbf{R}' \rangle \\ &\equiv h_{\mu \mathbf{R}, \mu' \mathbf{R}'}^0 + V_{\mu \mathbf{R}, \mu' \mathbf{R}'}(t). \end{aligned} \quad (65)$$

The second term is represented by

$$\begin{aligned} V_{\mu \mathbf{R}, \mu' \mathbf{R}'}(t) &= \langle \mu \mathbf{R} | \mathbf{F}(t) \cdot \mathbf{r} | \mu' \mathbf{R}' \rangle \\ &= \mathbf{F}(t) \cdot \mathbf{R} \delta_{\mu \mu'} \delta_{\mathbf{R} \mathbf{R}'} + \mathbf{F}(t) \cdot \mathbf{X}_{\mu \mu'} \bar{\delta}_{\mu \mu'} \delta_{\mathbf{R} \mathbf{R}'}, \end{aligned} \quad (66)$$

where \mathbf{X} is defined as the displacement of electron from the position of an ionic core of the crystal, namely, $\mathbf{X} = \mathbf{r} - \mathbf{R}$, and an electric dipole matrix element at each \mathbf{R} is approximately given by $\langle \mu \mathbf{R} | \mathbf{X} | \mu' \mathbf{R}' \rangle \approx \mathbf{r}_{\mu \mu'} \delta_{\mathbf{R} \mathbf{R}'}$ with $\mathbf{r}_{\mu \mu'} = \langle \mu | \mathbf{r} | \mu' \rangle$. Here, the property has been used that a Wannier function $\langle \mathbf{r} | \mu \mathbf{R} \rangle$ is just a function of \mathbf{X} and is mostly localized inside a cell situated at \mathbf{R} . Thus $\langle \mu \mathbf{R} | \mathbf{X} | \mu' \mathbf{R}' \rangle$ is considered almost independent of \mathbf{R} . Therefore, Eq. (43) is cast into

$$\begin{aligned} i \frac{\partial}{\partial t} \langle \mu \mathbf{R} | \hat{\Psi} \rangle &= \sum_{\mu' \mathbf{R}'} \{ h_{\mu \mathbf{R}, \mu' \mathbf{R}'}^0 + \mathbf{F}(t) \cdot (\mathbf{R} \delta_{\mu \mu'} \\ &\quad + \mathbf{r}_{\mu \mu'} \bar{\delta}_{\mu \mu'}) \delta_{\mathbf{R} \mathbf{R}'} \} \langle \mu' \mathbf{R}' | \hat{\Psi} \rangle. \end{aligned} \quad (67)$$

Now, the Peierls phase transform defined by

$$\langle \mu \mathbf{R} | \hat{\Psi} \rangle = e^{iA(t) \cdot \mathbf{R}} \langle \mu \mathbf{R} | \hat{\Phi} \rangle \quad (68)$$

brings Eq. (67) into the following equation for $\hat{\Phi}_{\mu \mathbf{R}} \equiv \langle \mu \mathbf{R} | \hat{\Phi} \rangle$ as

$$\sum_{\mu' \mathbf{R}'} e^{-iA(t) \cdot \mathbf{R}} \tilde{h}_{\mu \mathbf{R}, \mu' \mathbf{R}'}(t) e^{iA(t) \cdot \mathbf{R}'} \hat{\Phi}_{\mu' \mathbf{R}'} = i \frac{\partial}{\partial t} \hat{\Phi}_{\mu \mathbf{R}}, \quad (69)$$

where

$$\begin{aligned} \tilde{h}_{\mu \mathbf{R}, \mu' \mathbf{R}'}(t) &\equiv \langle \mu \mathbf{R} | \tilde{h}(t) | \mu' \mathbf{R}' \rangle \\ &= h_{\mu \mathbf{R}, \mu' \mathbf{R}'}^0 + \mathbf{F}(t) \cdot \mathbf{r}_{\mu \mu'} \bar{\delta}_{\mu \mu'} \delta_{\mathbf{R} \mathbf{R}'}. \end{aligned} \quad (70)$$

Here, $\tilde{h}(t)$ is defined by

$$\begin{aligned} \tilde{h}(\mathbf{r}, \mathbf{r}'; t) &= \langle \mathbf{r} | \tilde{h}(t) | \mathbf{r}' \rangle \\ &= \delta(\mathbf{r} - \mathbf{r}') h^0(\mathbf{r}) + \mathbf{F}(t) \cdot \boldsymbol{\chi}(\mathbf{r}, \mathbf{r}'), \end{aligned} \quad (71)$$

where

$$\chi(\mathbf{r}, \mathbf{r}') = \sum_{\mu\mu'\mathbf{R}} \langle \mathbf{r} | \mu\mathbf{R} \rangle \mathbf{r}_{\mu\mu'} \bar{\delta}_{\mu\mu'} \langle \mu'\mathbf{R} | \mathbf{r}' \rangle. \quad (72)$$

The following equation

$$\hat{\Phi}_{\mu\mathbf{k}}(t) \equiv \langle \mu\mathbf{k} | \hat{\Phi}(t) \rangle = \hat{a}_{\mu\mathbf{k}}(t) \quad (73)$$

is derived from Eq. (69), as shown in Appendix B, where $|\mu\mathbf{k}\rangle$ represents a Bloch state. Thus, by taking account of Eq. (68), $\hat{\Psi}(\mathbf{r}, t) = \langle \mathbf{r} | \hat{\Psi}(t) \rangle$ becomes of the form

$$\begin{aligned} \hat{\Psi}(\mathbf{r}, t) &= \frac{1}{\sqrt{N}} \sum_{\mu\mathbf{R}\mathbf{k}} \langle \mathbf{r} | \mu\mathbf{R} \rangle e^{i[\mathbf{k}+\mathbf{A}(t)]\cdot\mathbf{R}} \hat{a}_{\mu\mathbf{k}}(t) \\ &= \sum_{\mu\mathbf{k}} e^{i[\mathbf{k}+\mathbf{A}(t)]\cdot\mathbf{r}} U_{\mu[\mathbf{k}+\mathbf{A}(t)]}(\mathbf{r}) \hat{a}_{\mu\mathbf{k}}(t) \\ &\approx \sum_{\mu\mathbf{k}} e^{i[\mathbf{k}+\mathbf{A}(t)]\cdot\mathbf{r}} U_{\mu\mathbf{0}}(\mathbf{r}) \hat{a}_{\mu\mathbf{k}}(t) \\ &= \frac{1}{\sqrt{N}} \sum_{\mu\mathbf{R}\mathbf{k}} e^{i[\mathbf{k}+\mathbf{A}(t)]\cdot\mathbf{r}} \langle \mathbf{r} - \mathbf{R} | \chi_{\mu} \rangle \langle \chi_{\mu} | \hat{\psi}_{\mathbf{k}}(t) \rangle \\ &= \frac{1}{\sqrt{N}} \sum_{\mathbf{R}\mathbf{k}} e^{i[\mathbf{k}+\mathbf{A}(t)]\cdot\mathbf{r}} \langle \mathbf{r} - \mathbf{R} | \hat{\psi}_{\mathbf{k}}(t) \rangle. \end{aligned} \quad (74)$$

Here, in the second equality, a periodic part of the Bloch function $\langle \mathbf{r} | \mu\mathbf{k} \rangle$ is introduced as $U_{\mu\mathbf{k}}(\mathbf{r})$, in the third equality, the approximation of $U_{\mu\mathbf{K}(t)}(\mathbf{r}) \approx U_{\mu\mathbf{0}}(\mathbf{r})$ is made to be consistent with the spirit of the $\mathbf{k} \cdot \mathbf{p}$ model employed in Eq. (B6), and in the fourth equality, Eqs. (19) and (B7) are employed and the Wannier function $\langle \mathbf{r} | \mu\mathbf{R} \rangle$ is represented as $\langle \mathbf{r} - \mathbf{R} | \chi_{\mu} \rangle \equiv \chi_{\mu}(\mathbf{r} - \mathbf{R})$.

It is evident that the gauge transformation

$$\hat{\Psi}(\mathbf{r}, t) = e^{i\mathbf{A}(t)\cdot\mathbf{r}} \hat{\Psi}'(\mathbf{r}, t) \quad (75)$$

of Eq. (74) is attributed to the Peierls phase transform of Eq. (68), where

$$\hat{\Psi}'(\mathbf{r}, t) = \frac{1}{\sqrt{N}} \sum_{\mathbf{R}\mathbf{k}} e^{i\mathbf{k}\cdot\mathbf{r}} \hat{\psi}_{\mathbf{k}}(\mathbf{r} - \mathbf{R}, t). \quad (76)$$

Applying this to Eqs. (59) and (60), these become

$$\mathbf{M}(\mathbf{r}, t) = \mu_B g_e \langle \hat{\Psi}'^\dagger(\mathbf{r}, t) \mathbf{s} \hat{\Psi}'(\mathbf{r}, t) \rangle_g \quad (77)$$

and

$$\mathbf{M}^{(2)}(\mathbf{r}, t) = \mu_B \text{Re}[\langle \hat{\Psi}'^\dagger(\mathbf{r}, t) \{\mathbf{I} + \mathbf{r} \times \mathbf{A}(t)\} \hat{\Psi}'(\mathbf{r}, t) \rangle_g], \quad (78)$$

respectively. It is seen in Eq. (78) that the operator \mathbf{I} for the IFE is altered by an additional contribution depending on $\mathbf{A}(t)$, though the physical quantity $\mathbf{M}^{(2)}(\mathbf{r}, t)$ remains invariant with respect to this gauge transformation.

Finally, the volume-averaged magnetization at time t

$$\bar{\mathbf{M}}^{(\text{sol})}(t) = \bar{\mathbf{M}}(t) + \bar{\mathbf{M}}^{(2)}(t) \quad (79)$$

is shown below, where

$$\bar{\mathbf{M}}(t) = \frac{1}{V} \int d\mathbf{r} \mathbf{M}(\mathbf{r}, t), \quad (80)$$

with $\mathbf{M} = \mathbf{M}, \mathbf{M}^{(2)}$. Equation (77) becomes

$$\begin{aligned} \bar{\mathbf{M}}(t) &= \frac{\mu_B g_e}{V} \sum_{\mathbf{k}\mu\nu\Delta\mathbf{R}} \int dX \chi_{\mu}^*(X) \mathbf{s} \chi_{\nu}(X + \Delta\mathbf{R}) \langle a_{\mathbf{k}\mu}^\dagger(t) a_{\mathbf{k}\nu}(t) \rangle_g \\ &\approx \frac{\mu_B g_e}{V} \sum_{\mathbf{k}\mu\nu} \rho_{\mathbf{k}\mu\nu}(t) \langle \mu | \mathbf{s} | \nu \rangle, \end{aligned} \quad (81)$$

where in the last equality just the Wannier functions at the same site, namely, $\Delta\mathbf{R} = \mathbf{0}$, are taken account of for the summation over $\Delta\mathbf{R}$ and the density matrix of Eq. (21) is introduced. Similarly, Eq. (78) ends up with

$$\bar{\mathbf{M}}^{(2)}(t) = \frac{\mu_B}{V} \sum_{\mathbf{k}\mu\nu} \text{Re}[\rho_{\mathbf{k}\mu\nu}(t) \{ \langle \mu | \mathbf{I} | \nu \rangle + \langle \mu | \mathbf{r} | \nu \rangle \times \mathbf{K}(t) \}], \quad (82)$$

with $\mathbf{K}(t) = \mathbf{k} + \mathbf{A}(t)$. By numerically evaluating $\bar{\mathbf{M}}^{(\text{sol})}(t)$ at each t , the temporal variance of it is examined, followed by extracting the time-independent magnetization at the asymptotic limit, $\bar{\mathbf{M}}^{(\text{sol})}(t \rightarrow \infty)$. In actual calculations, the expression of Eq. (35) for the density matrices is employed in light of Eqs. (38) and (39).

III. RESULTS AND DISCUSSION

A. Floquet energy bands and Weyl node formation

For the purpose of the later discussion of induced magnetization, one shows the band structures of Floquet energy $E_{\alpha}(\mathbf{k})$ that are calculated based on the theoretical framework of Sec. II A. For the numerical calculations, the same material parameters as those of Ref. [59] are employed; the band gap of the original crystal Zn_3As_2 is set to be $E_g = 0.0169$ (0.46 eV). Hereafter, the conduction bands with $J_z = \pm 1/2$ and the heavy-hole bands with $J_z = \pm 3/2$ are denoted as e and hh , respectively, and thus the associated Floquet sidebands with N photons are represented by $e(N)$ and $hh(N)$, respectively. In particular, attention is paid to the Floquet states of $e(0)$, $e(-1)$, $hh(0)$, and $hh(+1)$ around the Fermi energy $E_F = 0$, which is set at the middle of the energy difference between the original e and hh bands at the Γ point. It is likely that the band of $e(-1)$ crosses with that of $hh(+1)$ in a certain range of laser frequency ω and strength of electric field F_c to form a pair of Weyl nodes on the k_z axis, accompanying band deformation. Strictly speaking, pairs of Weyl nodes manifest themselves in many places in the BK, at which the Floquet bands $e(N)$ and $hh(N')$ intersect regardless of the magnitude of $\omega (\neq 0)$; for more detail, consult Fig. 6 of Ref [59].

Figure 1(a) shows the variance of locations of the Weyl nodes at $k_z^{W(+)}$ and $k_z^{W(-)}$ on the k_z axis for up-spin and down-spin states of FWSM, respectively, as a function of F_c with $\omega = 0.0147$ (0.4 eV). Figure 1(b) shows the same as Fig. 1(a) but as a function of ω with $F_c = 0.0003$ (1.54 MV/cm). It is found that one Weyl node at $k_z^{W(\pm)}$ is annihilated with another Weyl node formed at $-k_z^{W(\pm)}$ with an opposite chirality at $k_z^{W(\pm)} = 0$ where these are brought together. This shows a topological phase transition to a trivial insulating phase with the opening of a Floquet band gap. Another topological phase transition to a nontrivial insulating phase at $k_z^{W(\pm)} = \pi$ would be likely caused for $\omega > E_g$ as shown in Fig. 1(b), while this

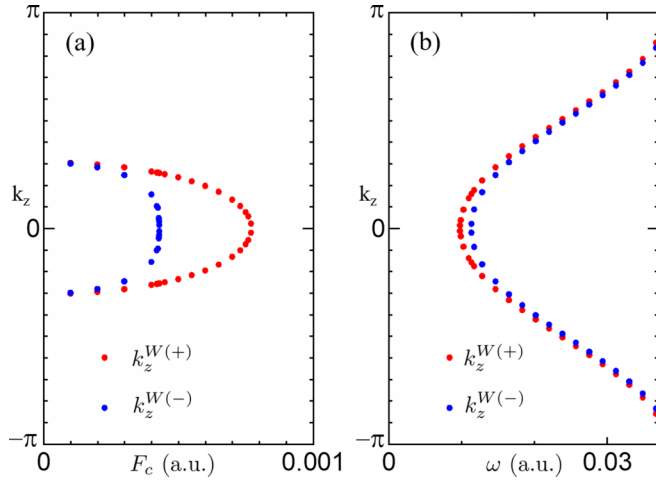


FIG. 1. Variance of locations of the Weyl nodes at $k_z^{W(+)}$ and $k_z^{W(-)}$ on the k_z axis for up-spin (denoted by red dots) and down-spin (denoted by blue dots) states of FWSM, respectively. (a) $k_z^{W(\pm)}$ as a function of F_c with $\omega = 0.0147$ (0.4 eV). The axis of ordinate is gauged in the unit of $1/d_z$. (b) The same as panel (a) but as a function of ω with $F_c = 0.0003$ (1.54 MV/cm).

is not verified in Fig. 1(a), where $k_z^{W(\pm)} = 0.95$ at $F_c \rightarrow 0$ following an analytic model derived in Ref. [59]. The variance of locations of the Weyl nodes is consulted in Sec. III B for the discussion of the F_c and ω dependence of the induced magnetization.

Figures 2(a) and 2(b) show bulk energy dispersions of $E(\mathbf{k})$ of up-spin and down-spin FWSM bands of $e(-1)$ and $hh(+1)$ at $k_z = 0$, respectively, where $F_c = 0.0003$ (1.54 MV/cm) and $\omega = 0.0147$ (0.4 eV) that is almost resonant with the band gap E_g . The opening of Floquet band gap is confirmed in both panels; in fact, these bands remain open besides $k_z = 0$ as far as $-k_z^{W(\pm)} < k_z < k_z^{W(\pm)}$. It is seen that the up-spin Floquet band of $e(-1)$ looks almost degenerate with that of $hh(-1)$, accompanying the formation of a nodal ring reminiscent of the Floquet nodal-line SM, in contrast with the down-spin Floquet band showing the clear band gap formation. The difference is attributed to the fact that optical transitions between bands with down spin are more dominantly made than those with up spin by the left-hand circularly polarized laser, as mentioned in Sec. I. To be more specific, the band gap of the up-spin Floquet band arises from an optical spin-orbit coupling, namely, a spin-orbit coupling t_{sp} reduced by a factor of $J_1(z_c)$ with $z_c = F_c d_c / \omega$ and $d_c \equiv d_x = d_y$, while that of the down-spin band is governed by an optical dipole coupling $\Omega_c (\equiv \Omega_x = \Omega_y)$, where $t_{sp} J_1(z_c) = 2.1 \times 10^{-4}$ and $\Omega_c = 5.5 \times 10^{-3}$ [59]. As ω increases from E_g , the dominance of the down-spin bands becomes more suppressed and, eventually, the difference between these two would disappear for $\omega \gg E_g$. Here is one more comment on the nodal ring of the up-spin Floquet band. The energy dispersion $E^{(+)}(\mathbf{k})$ at any k_z has the similar structure as that of Fig. 2(a) at $k_z = 0$ as long as $|k_z| < k_z^{W(+)}$, apart from the fact that the positions of the rings shift upward in energy from $E_F = 0$ and the diameters of the rings decrease as k_z increases. Eventually, the ring converges to the Weyl node with vanishing of the diameter. By connecting these rings as functions of k_z continuously, one can imagine that

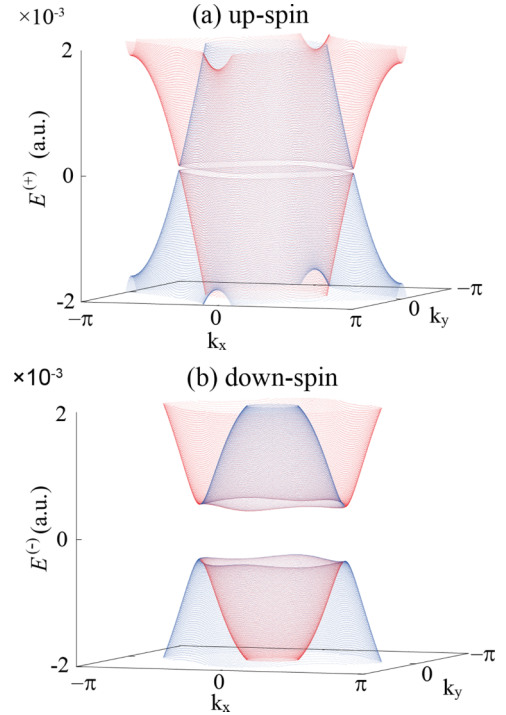


FIG. 2. Bulk energy dispersion of $E^{(\pm)}(\mathbf{k})$ of FWSM bands of $e(-1)$ and $hh(+1)$ at $k_z = 0$ in the atomic units, generated by the laser drive with circular polarization, where $F_c = 0.0003$ (1.54 MV/cm) and $\omega = 0.0147$ (0.4 eV). Here, bands dominated rather by the s -orbital (p -orbital) component are denoted by a red (blue) solid line. The axis of abscissa k_l is gauged in the unit of $1/d_l$ with $l = x, y$. (a) $E^{(+)}(\mathbf{k})$ in the $k_x - k_y$ plane for the up-spin bands. (b) $E^{(-)}(\mathbf{k})$ in the $k_x - k_y$ plane for the down-spin bands. (This figure is quoted from Fig. 7 of Ref. [59] after some processing.)

the intersection between $e(-1)$ and $hh(+1)$ bands forms a manifold similar to a spheroid in the BZ with the k_x and k_y axes as two principle axes with the same length and a line connecting a pair of Weyl nodes, namely, the k_z axis as the third axis.

Hereafter, it is understood that an open boundary condition is imposed on the Floquet eigenvalue equation of Eq. (12) in the y direction in place of the periodic one, where an electron is confined within a finite range of y , while moving freely in the $x - z$ plane. The resulting band of α state is represented as $\mathcal{E}_\alpha(\bar{\mathbf{k}})$ with $\bar{\mathbf{k}} = (k_x, k_z)$ to make it distinct from $E_\alpha(\mathbf{k})$, where $\mathcal{E}_\alpha(\bar{\mathbf{k}})$ is considered as a projection of $E_\alpha(\mathbf{k})$ onto the $k_x - k_z$ plane. The confinement of electron results in the formation of surface states within the band gaps seen in Figs. 2(a) and 2(b). Figure 3 is a schematic view of FWSM band structures, $\mathcal{E}^{(+)}(\bar{\mathbf{k}})$ and $\mathcal{E}^{(-)}(\bar{\mathbf{k}})$, for the up-spin and down-spin states, respectively, which is depicted based on the results of the numerical calculations of Eq. (12) under the open boundary condition. Figures 3(a) and 3(b) show the surface states pinned to a pair of Weyl nodes at $\bar{\mathbf{k}}^{W(\pm)} \equiv (0, k_z^{W(\pm)})$ and $-\bar{\mathbf{k}}^{W(\pm)}$ and exhibiting a Fermi arc if all electrons are assumed to be occupied below E_F . Here it is also shown that the height of the up-spin Weyl cones is much smaller than that of the down-spin Weyl cones due to the same reason as the difference of the band gap between Figs. 2(a) and 2(b). In Figs. 3(c)/3(d), the

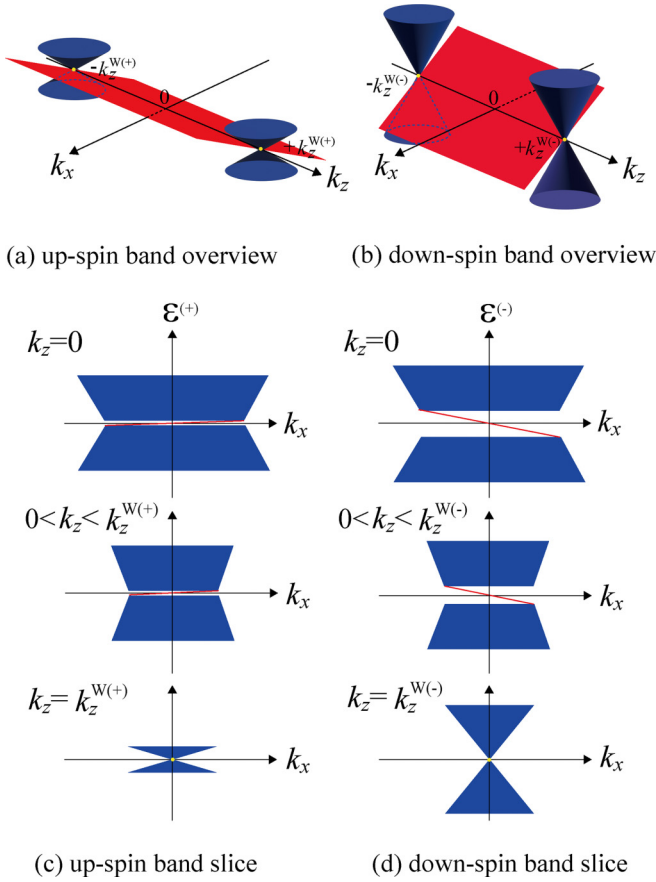


FIG. 3. Schematic view of band structures of FWSM for both spin states. (a) Overview of the up-spin band with a surface state (painted in red) pinned to a pair of Weyl nodes at $\pm k_z^{W(+)}$ (specified in yellow), which are formed as intersections of Dirac cones (painted in blue). (b) The same as panel (a) but for the down-spin band. (c) Energy dispersions of the up-spin band $\mathcal{E}^{(+)}$ as functions of k_x , sliced at $k_z = 0$, k_z with $0 < k_z < k_z^{W(+)}$, and $k_z = k_z^{W(+)}$. The projected bulk bands are painted in blue and the surface states are depicted by red solid lines. (d) The same as panel (c) but energy dispersions of the down-spin band $\mathcal{E}^{(-)}$.

energy dispersion $\mathcal{E}^{(+)} / \mathcal{E}^{(-)}$ of the up-spin/down-spin band is sliced at three different k_z 's, namely, $k_z = 0$, k_z located between 0 and $k_z^{W(+)} / k_z^{W(-)}$, and $k_z = k_z^{W(+)} / k_z^{W(-)}$, and these sliced energy bands are shown as functions of k_x . The range of line segment in the k_x axis that supports a surface state is maximized at $k_z = 0$, and more reduced with increasing k_z from 0 to $k_z^{W(\pm)}$. Incidentally, connecting these line segments in Fig. 3(c) continuously from $-k_z^{W(+)}$ to $+k_z^{W(+)}$ leads to a manifold similar to an ellipse formed in the $k_x - k_z$ plane; obviously, this is nothing but the projection of the manifold mentioned above for $E^{(+)}(\mathbf{k})$.

These surface states play decisive roles of generating solenoid magnetization $\bar{M}^{(\text{sol})}(t)$ of Eq. (79) in this study, as shown below. This is because the main part of the spin magnetization $\bar{M}(t)$ is caused due to the imbalance between excited carrier densities in the up-spin band and those in the down-spin band. Here, the degree of imbalance corresponds to the degree of spin polarization, denoted as I_{spin} , which is defined as the ratio of the spin difference to the total number

of electrons. Such imbalance is considered more conspicuous than that in the bulk states, since most of the electrons in the bulk still stay at the parent band $hh(0)$ associated with the ground state in spite of the intense optical excitation of concern.

B. Surface magnetization

The excited electron densities at time t in the bulk and surface are evaluated by the volume average density $\eta_{ee}^{(b)}(t)$ and the surface average density $\eta_{ee}^{(s)}(t)$, respectively. These are the diagonal components of $\eta_{\mu\nu}^{(b)}(t)$ and $\eta_{\mu\nu}^{(s)}(t)$ defined in terms of $\rho_{k\mu\nu}(t)$, as shown in Eqs. (C3) and (C5), respectively. The surface magnetization is provided by replacing Eqs. (81) and (82) by alternative expressions suitable for the generation of the surface states, which is read as Eq. (C6), that is,

$$\bar{M}^{(\text{sol})}(t) = \mu_B \text{Re} \sum_{\mu\nu} \eta_{\mu\nu}^{(s)}(t) \langle \mu | g_e \mathbf{s} + \mathbf{l} + \mathbf{r} \times \mathbf{A}(t) | \nu \rangle. \quad (83)$$

It is found that this is composed of the three contributions from the spin magnetization, the orbital magnetization relevant to the IFE, and the remaining term due to the gauge correction. Here, the z component of it, $\bar{M}_z^{(\text{sol})}(t)$, is evaluated.

Figure 4(a) shows $\eta_{ee}^{(b)}(t)$'s for both spins as functions of t with the relaxation times introduced in Eqs. (38) and (39) as $T_1 = 500$ fs and $T_2 = 250$ fs, respectively, where $F_c = 0.0003$ (1.54 MV/cm) and $\omega = 0.0147$ (0.4 eV). The total valence electron density of the crystal amounts to $n_e = 4.4 \times 10^{22} \text{ cm}^{-3}$. The red and blue solid lines represent one-cycle time (T) average of these electron densities of down spin and up spin, respectively, and $I_{\text{spin}} \approx 0.01$ at $t = 25T$, where one period equals $T = 10.3$ fs. Figure 4(b) shows $\eta_{ee}^{(s)}(t)$'s for both spins as functions of t , where surface electron states are extracted from all of the calculated Floquet states numerically by inspecting the degree of electron densities localized at the outermost site in the y direction. The incorporated surface states are shown in Figs. 4(c) and 4(d). It is remarked that, for the purpose of comparison with $\eta_{ee}^{(b)}(t)$ of Fig. 4(a), $\eta_{ee}^{(s)}(t)$ of Fig. 4(b) is shown in the unit of cm^{-3} by dividing $\eta_{ee}^{(s)}(t)$ defined in Eq. (C5) by the lattice constant $d_y = 3 \text{ \AA}$ in the y direction instead of the usual unit of cm^{-2} . Here, it is found that $I_{\text{spin}} \approx 0.5$ at $t = 25T$, which is much greater than that in the bulk. The surface electron densities created by the drive with the linear polarization show no spin difference between both excited electron densities, as is clear (though not shown here).

Figure 5(a) shows the calculated result of the induced surface magnetization (represented by a solid black line), where the one-cycle average value is represented by a solid red line, and the magnetic induction, namely, the magnetization multiplied by μ_0 , $B_z^{(\text{ind})}(t) \equiv \mu_0 \bar{M}_z^{(\text{sol})}(t)$, is gauged in the unit of mT, where $\eta_{\mu\nu}^{(s)}(t)$ appearing in Eq. (83) is redefined by dividing by d_y . It is found that the magnetization of the order of 1 mT is induced in the present system. This strength seems compatible with the rough estimate that $\eta_{ee}^{(s)}(t)$ is about one thousand times smaller than n_e , where assuming all electrons of the crystal are aligned as an ideal ferromagnet the magnetization of the order of 1 T is generated besides the IFE. In passing, the strength of a refrigerator magnet is of the order of mT. The detailed origins of the induced magnetization are

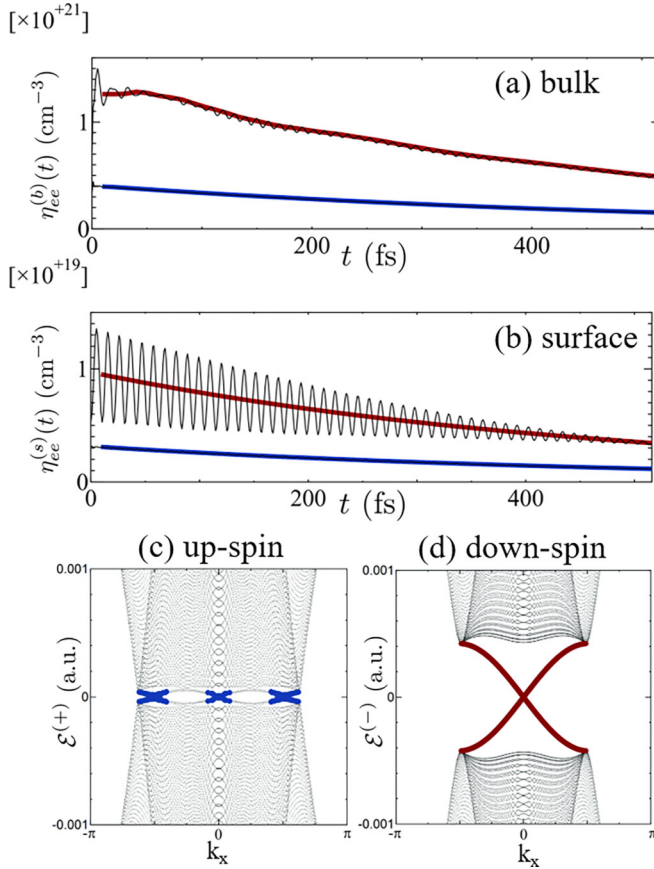


FIG. 4. (a) Excited electron densities in the bulk $\eta_{ee}^{(b)}(t)$ (in the unit of cm^{-3}) for both spins as functions of time t (in the unit of fs), where $F_c = 0.0003$ (1.54 MV/cm) and $\omega = 0.0147$ (0.4 eV). The red and blue solid lines represent one-cycle time average of these electron densities of down spin and up spin, respectively. (b) The excited electron densities in the surface $\eta_{ee}^{(s)}(t)$ (cm^{-3}) for both spins as functions of t (fs), where $F_c = 0.0003$ (1.54 MV/cm) and $\omega = 0.0147$ (0.4 eV). Here, these densities are gauged in the unit of cm^{-3} rather than cm^{-2} . For more detail, consult the text. (c) Surface states incorporated with the calculation of $\eta_{ee}^{(s)}(t)$ for the up spin, represented by blue solid lines, are shown overlaid on $\mathcal{E}^{(+)}(\vec{k})$ as a function of k_x with $k_z = 0$. (d) The same as panel (c) but for the down spin, represented by red solid lines, are shown overlaid on $\mathcal{E}^{(-)}(\vec{k})$ as a function of k_x with $k_z = 0$.

analyzed by examining the respective contributions from the three different generation mechanisms, which are shown in Figs. 5(b)–5(d). It is seen that the negative values of the spin magnetization and the orbital magnetization, namely, the IFE, are in harmony with the dominance of $\eta_{ee}^{(s)}(t)$ of the down spin with $J_z = -1/2$ over that of the up spin with $J_z = 1/2$, as shown in Fig. 4(b). To be more precise, $\eta_{hh}^{(s)}(t)$ of the down spin with $J_z = -3/2$ also contributes to these magnetizations, since the down-spin Floquet bands are formed by the hybridization between the two bands with $J_z = -1/2, -3/2$ through both the spin-orbit and electric-dipole couplings. The contributions of the IFE to $B_z^{(\text{ind})}(t)$ are always slightly smaller than those of the spin magnetization regardless of F_c to the extent examined. On the other hand, the magnetization due to the gauge correction oscillates violently immediately after the

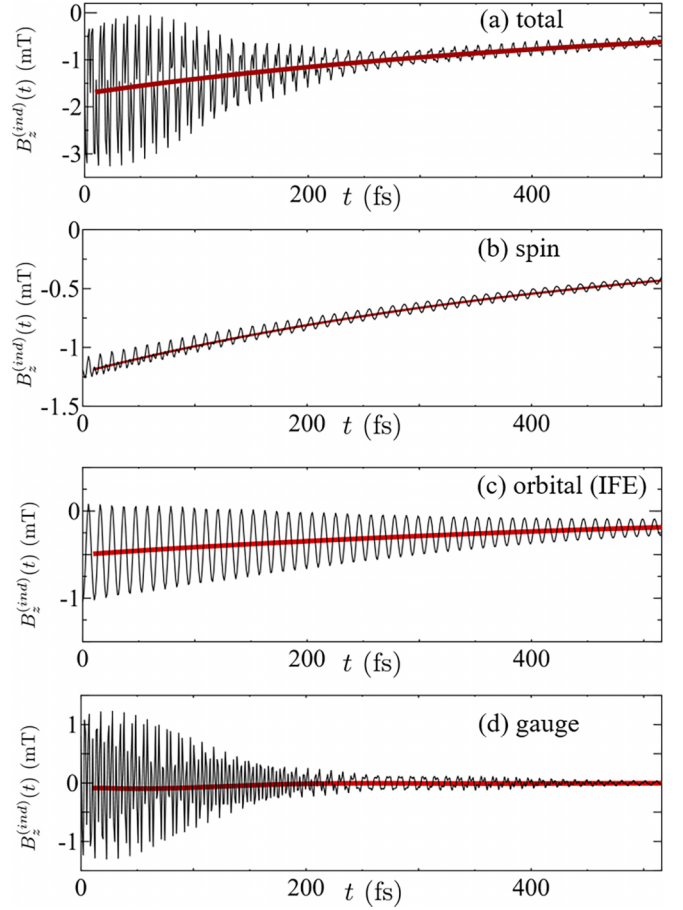


FIG. 5. (a) Surface magnetic induction $B_z^{(\text{ind})}(t)$ (in the unit of mT), represented by a solid black line, as a function of time t (in the unit of fs), where $F_c = 0.0003$ (1.54 MV/cm) and $\omega = 0.0147$ (0.4 eV). Here, the one-cycle average value is represented by a solid red line. For more detail, consult the text. (b) The same as panel (a), but for the surface magnetization attributed to the spin magnetization. (c) The same as panel (a), but for the surface magnetization attributed to the orbital magnetization associated with the IFE. (d) The same as panel (a), but for the surface magnetization attributed to the gauge correction term.

excitation, but asymptotically becomes negligibly small. Such a tendency of this correction term remains largely unchanged regardless of F_c to the extent examined. On the other hand, it would be worth mentioning here the induced magnetization of bulk. According to numerical calculations of $\vec{M}^{(\text{sol})}(t)$ with modification from Eq. (83) for the bulk, the induced magnetization is estimated to be about 40 mT at $t = 25T$ as a mere ideal maximum [92]. The most contribution comes from the IFE, though both the spin magnetization and the gauge correction have little effect.

Here, the surface magnetic induction of the IFE imparted by $B_z^{(\text{ind})}$, which is represented as $B_z^{(\text{IFE})}$, is discussed in a qualitative manner in terms of the expression of IFE based on the Drude-Lorentz model. This is read as [81]

$$B_z^{(\text{IFE})} = -\frac{\mu_0 n_e^{(s)}(F_c)}{2} \frac{\omega}{(\omega^2 - \omega_0^2)^2 + (\gamma\omega)^2} F_c^2, \quad (84)$$

where $n_e^{(s)}(F_c)$ represents a surface electron density; ω_0 and $1/\gamma$ represent a resonance energy and a transverse relaxation time, respectively. It is noted that the electrons occupied in the surface states are composed of a portion of excited carriers in the present FWSM system and thus the leading contribution of $n_e^{(s)}(F_c)$ arises from F_c^2 terms, namely, $n_e^{(s)}(F_c) \propto F_c^2$. This implies that $B_z^{(\text{IFE})}$ of concern would be dominated by the F_c^4 terms, differing from the conventional IFE depending on F_c^2 . Here, it would be appropriate to set ω_0 equal to zero, since the FWSM surface states are considered metallic. Thus, with $n_e^{(s)}(F_c) \approx 0.5 \times 10^{19} \text{ cm}^{-3}$, $\omega = 0.4 \text{ eV}$, $F_c = 1.54 \text{ MV/cm}$, and $1/\gamma = T_2 = 250 \text{ fs}$, one obtains $B_z^{(\text{IFE})} \approx -2.5 \text{ mT}$. The results of Fig. 5(c) are somehow consistent with this estimate. Incidentally, the magnitude of it is about similar to that of a disordered metal, though under a different optical condition [76].

Next, the discussion is made on the F_c dependence of the surface magnetization with $\omega = 0.0147$ (0.4 eV). The variance of locations of the Weyl nodes for both spin states with respect to F_c is shown in Fig. 1(a), where it is seen that the Weyl node moves from the band center at $k_z = 0$ toward the band edge as F_c decreases. Figures 6(a) and 6(b) show $\eta_{ee}^{(s)}(t)$ and $B_z^{(\text{ind})}(t)$ at $F_c = 0.0001$ (0.51 MV/cm), respectively, and Figs. 6(c) and 6(d) show those at $F_c = 0.0002$ (1.03 MV/cm). These correspond to Figs. 4(b) and 5(a) for $F_c = 0.0003$. The projected Floquet bands $\mathcal{E}(\vec{k})$ in both cases of F_c look similar to those of Figs. 4(c) and 4(d) besides the size of band gap at $k_z = 0$ (though not shown here). It is obvious that $\eta_{ee}^{(s)}(t)$ at $F_c = 0.0002$ is much more dominant over that at $F_c = 0.0001$, which is reflected on the difference between $B_z^{(\text{ind})}(t)$'s in both cases in a straightforward manner. It is noted that the magnitude of $B_z^{(\text{ind})}(t)$ at $F_c = 0.0002$ is noticeably larger than that at $F_c = 0.0003$. This is understood from the perspective of the degree of spin polarization I_{spin} , that is, $I_{\text{spin}} \approx 1$ at $F_c = 0.0002$ even though $\eta_{ee}^{(s)}(t)$ for the down spin is of a comparable order with that at $F_c = 0.0003$. As F_c increases from 0.0003, the magnitude of $B_z^{(\text{ind})}(t)$ becomes smaller. Further, the direction of it changes to the positive sign when F_c exceeds around 0.0004, since the pair of Weyl nodes of the down spin is annihilated at $k_z = 0$ to cause the disappearance of the surface states, as shown in Fig. 1(a).

As regards the ω dependence of the surface magnetization with $F_c = 0.0003$ (1.54 MV/cm), the variance of locations of the Weyl nodes for both spin states with respect to ω is shown in Fig. 1(b), where it is seen that the Weyl node moves from the band center toward the band edge as ω increases. Figure 7(a) shows $B_z^{(\text{ind})}(t)$ at $\omega = 0.0110$ (0.3 eV). Here, the up spin band forms a pair of Weyl nodes, whereas a gap still opens in the down spin band, accompanying a trivial insulating phase, as seen in Figs. 7(b) and 7(c). This is consistent with the observation that the resulting magnetization is oriented in a positive direction with much smaller magnitude than that seen in Fig. 5(a) at $\omega = 0.4 \text{ eV}$.

As ω increases above the band gap $E_g = 0.46 \text{ eV}$, the picture changes dramatically, as shown for $\omega = 0.5 \text{ eV}$ in Fig. 8. As mentioned in Sec. III A, the Floquet bands of $\mathcal{E}_{e(-1)}(\vec{k})$ and $\mathcal{E}_{hh(+1)}(\vec{k})$ form the pairs of Weyl nodes at $k_z = k_z^{(\pm)}, -k_z^{(\pm)}$ accompanying the surface states for $\omega < E_g$. Here, bands are arranged in ascending order in energy as $hh(0)$, $e(-1)$, $hh(+1)$, and $e(0)$ in the whole

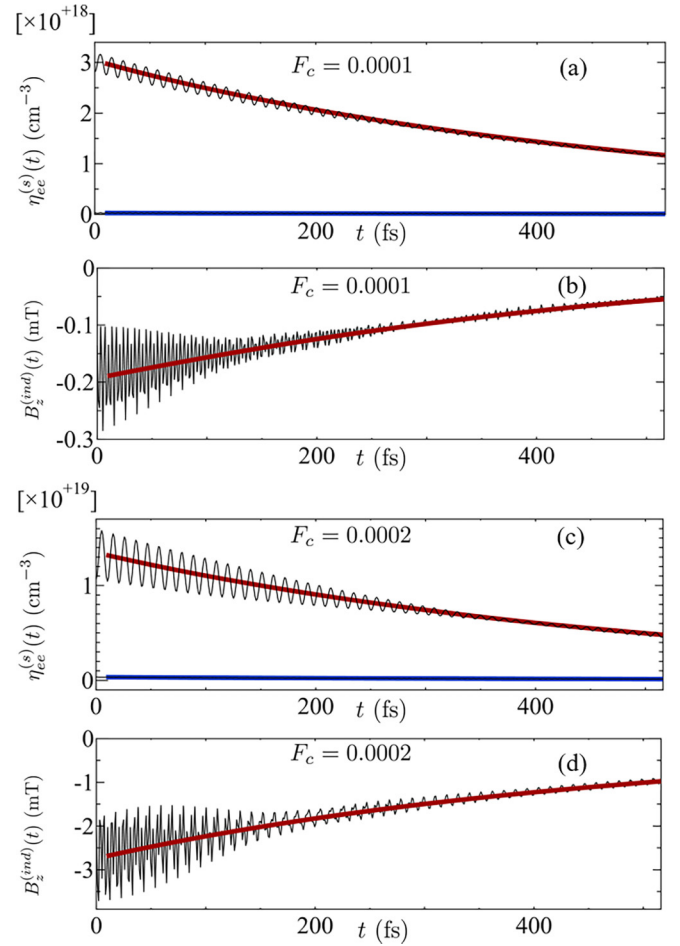


FIG. 6. F_c dependence of the excited electron densities in the surface $\eta_{ee}^{(s)}(t)$ and the surface magnetic induction $B_z^{(\text{ind})}(t)$ with $\omega = 0.0147$ (0.4 eV). (a),(b) The same as Fig. 4(b) and Fig. 5(a), respectively, but for $F_c = 0.0001$ (0.51 MV/cm). (c),(d) The same as Fig. 4(b) and Fig. 5(a), respectively, but for $F_c = 0.0002$ (1.03 MV/cm).

two-dimensional BZ. However, when $\omega > E_g$, it is expected that these bands are rearranged in the order of $e(-1)$, $hh(0)$, $e(0)$, and $hh(+1)$ in the limited region of the BZ including $\vec{k} = \mathbf{0}$. Figure 8(c) for the down-spin bands is the case. Here, a pair of bands of $hh(+1)$ and $e(0)$ repel with each other strongly, forming a conspicuous anticrossing due to the optical dipole coupling without surface states, and so do another pair of bands of $hh(0)$ and $e(-1)$. Further, the bottom of band $e(0)$ lies above the top of band $h(0)$, forming a band gap around $E_F = 0$. In the remaining region of the BZ, a band gap is still formed by the bands of $e(-1)$ and $hh(+1)$ around $E_F = 0$, supporting surface states extending to the edges of the BK. As regards the up-spin bands seen in Fig. 8(b), the band rearrangement does not occur yet, and the bottom of band $hh(+1)$ lies above the top of band $e(-1)$, which reduces the region of the BK where the surface states are allowed to exist. The resulting magnetization is shown in Fig. 8(a) and this is larger than that in Fig. 6(d), presumably due to enhancement of I_{spin} .

Roughly speaking, the magnetization $B_z^{(\text{ind})}(t)$ is considered proportional to the product of $\eta_{ee}^{(s)}(t)$ of down-spin

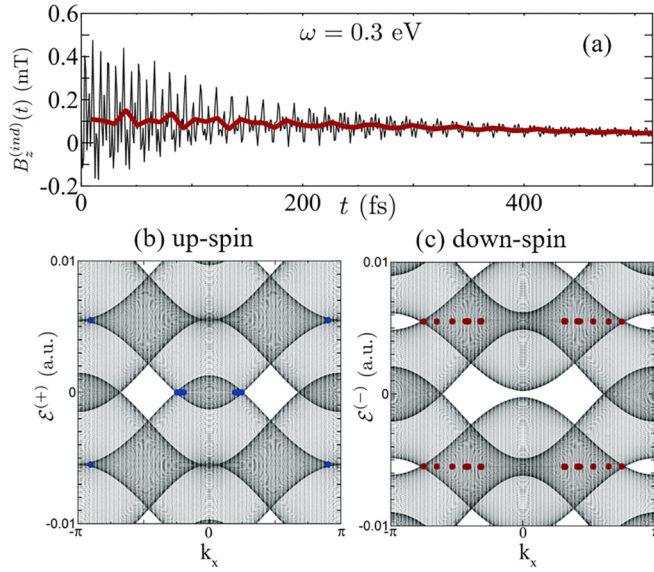


FIG. 7. ω dependence of the surface magnetic induction $B_z^{(\text{ind})}(t)$ with $F_c = 0.0003$ (1.54 MV/cm). (a) The same as Fig. 5(a) but for $\omega = 0.0110$ (0.3 eV). (b) Surface states incorporated with the calculation of $B_z^{(\text{ind})}(t)$ for the up spin, represented by blue dots, similar to Fig. 4(c). (c) Surface states incorporated with the calculation of $B_z^{(\text{ind})}(t)$ for the down spin, represented by red dots, similar to Fig. 4(d).

electrons and an area of the associated surface state A_W , where A_W corresponds to the area in the BZ that is painted in red in Figs. 3(b). Assuming that the shape of the surface state in the BZ is an ellipse, as mentioned in Sec. III A, this area is approximately represented as

$$A_W = \frac{\pi K_x K_z}{\cos \theta_W}, \quad (85)$$

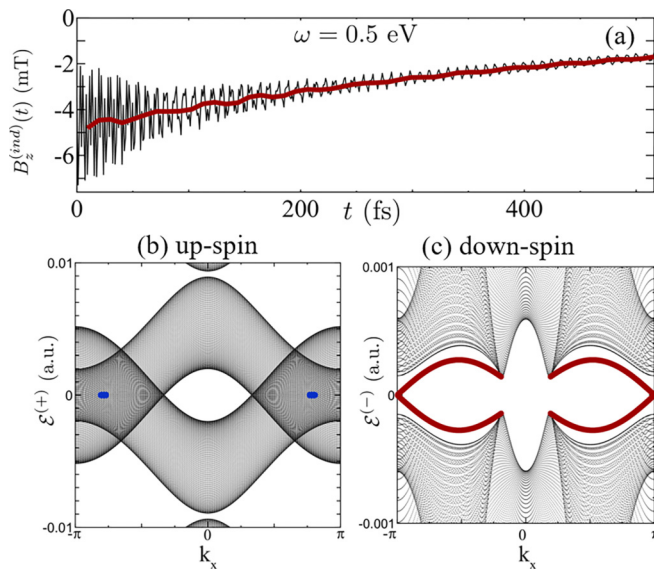


FIG. 8. ω dependence of the surface magnetic induction $B_z^{(\text{ind})}(t)$ with $F_c = 0.0003$ (1.54 MV/cm). (a) The same as Fig. 7(a) but for $\omega = 0.0184$ (0.5 eV). (b) The same as Fig. 7(b) but for $\omega = 0.0184$ (0.5 eV). (c) The same as Fig. 7(c) but for $\omega = 0.0184$ (0.5 eV).

where K_z is half of the separation of the pair of Weyl nodes, given by $K_z = k_z^{W(-)}$, K_x is half of the line segment in the k_x axis that supports the down-spin surface state at $k_z = 0$, and θ_W is an intersection angle between the down-spin surface plane in the BZ and the $k_x - k_z$ plane. That is,

$$B_z^{(\text{ind})}(t) \propto \eta_{ee}^{(s)}(t) A_W. \quad (86)$$

This is considered correct under restricted conditions that $\omega \approx E_g$ and $F_c \lesssim 0.0003$, corresponding to the cases of Figs. 5(a), 6(a), and 6(c). Otherwise, the expression of A_W can be modified to a certain extent and $B_z^{(\text{ind})}(t)$ would be of a more complicated form. Actually, anticrossings formed in the region of $\omega > E_g$ hinder the formation of the surface state around $k_x = 0$ in part, which corresponds to the case of Fig. 8(a). However, the separation K_z would still play an important role in the formation of magnetization, since K_z becomes greater with the increase of ω , as seen in Fig. 1(b). In summary, it is speculated that K_z is a crucial factor governing the surface magnetization. Incidentally, this factor also plays a key role of the anomalous Hall effect that is expected to be realized in the present FWSMs [4,23–27], though this is beyond the scope of this paper.

IV. CONCLUSIONS

The nonmagnetic and narrow-gap semiconductor Zn_3As_2 is driven by a left-hand circularly polarized continuous-wave laser with a nearly resonant frequency to the band gap to produce the two types of FWSM phases distinguished by the spins. The numerical evaluation of the transient nonequilibrium dynamics of the concerned system shows that the FWSM surface state formation accompanies the surface magnetization composed of the spin polarization and the orbital magnetization corresponding to the IFE with the gauge correction. The magnitude and direction of the magnetization varies sharply, depending on the intensity and frequency of the driving laser. It is stressed that the surface magnetization found here is more pronounced, when the laser has a nearly resonant frequency, and this is strong enough to form distinct Weyl pairs in the BK and to make the occupied electrons in the surface states highly spin polarized. Such an intriguing phenomenon would be measurable by virtue of the longitudinal magneto-optic Kerr effect appropriate for detecting surface magnetization [93–95]. However, it is remarked that, in actual experiments, the high-intensity laser employed here would possibly lead to effects of disturbing the predicted magnetization due to heating, spin relaxation through a coupling with phonons and a spin-spin interaction, band gap renormalization, and so on, which are not considered here.

The findings in this paper have the following significance. The laser-induced magnetization presented here is a departure from conventional research on photoinduced magnetization [60,69–71,75–80] in that, in the former, the surface magnetization separated from bulk magnetization is enhanced by spin magnetization due to high-density resonant excitation in addition to the IFE, while, in the latter, this is due to spin flips simply caused by the IFE in coordination with a strong spin-orbit coupling. Such induced magnetization is expected to provide a new platform for the studies of magnetotransport in topological materials. For instance, this would enable optical

control of chiral anomaly that is still a less studied issue [96]. To be more specific, it is likely that the surface magnetization is further fed back to an interaction with electronic states of a pair of FWSMs to form Landau levels in the k_z direction in a realistic situation, though this is disregarded in the theoretical model employed here. Application of an additional electric field along the z direction is considered to exhibit negative magnetic resistance due to the chiral anomaly that is dominantly shown in a relatively low magnetic field region corresponding to that evaluated here [24,28–31].

Finally, one more comment is made on the advantage of the theoretical method developed here to deal with the nonequilibrium dynamics of the Floquet topological systems. To deepen the understanding of these systems in nonequilibrium and to further explore the underlying physics of it, an approach from the transient quantum dynamics accompanying real carrier excitation is inevitably required in addition with just the analyses of Floquet band structures. In this study, by introducing the creation and annihilation operators of a fermionic quasiparticle, represented as $\hat{b}_{k\alpha}^{\dagger}(t)$ and $\hat{b}_{k\alpha}(t)$, respectively, a density matrix $\rho_{k\mu\nu}(t) = \langle \hat{a}_{k\mu}^{\dagger}(t) \hat{a}_{k\nu}(t) \rangle_g$ can be represented in a closed form without numerically solving the optical Bloch equations. Here, the fermionic quasiparticle is considered as a composite particle in which laser-electron interactions are fully renormalized to a band electron in terms of the Floquet base. Thus it is expected that these fermionic quasiparticle operators can be employed to facilitate the description of the nonequilibrium dynamics of the topological materials driven by a laser pulse with a relatively long temporal width of the order of ps. Actually, a variety of the Keldysh Green's functions [97] are described in closed forms in a nonperturbative manner with respect to a laser-electron interaction and these are specifically applied to high-harmonic generation, high density excitation, etc. Further, based on these operators, it is also possible to construct the Green's functions incorporating electron correlation effects for examining many-body effects of Floquet topological materials that still remain unexplored.

APPENDIX A: MISCELLANEOUS RELATIONS DERIVED FROM THE FLOQUET EIGENVALUE EQUATIONS

The Floquet eigenvalue equations are represented by the following equations as

$$\sum_{\nu} L_{F\mu\nu}(\mathbf{k}, t) \varphi_{\nu, k\alpha}(t) = E_{\alpha}(\mathbf{k}) \varphi_{\mu, k\alpha}(t) \quad (\text{A1})$$

and

$$\sum_{\nu\nu'} L_{F\mu\nu, \nu\nu'}(\mathbf{k}) C_{\nu\nu', k\alpha} = E_{\alpha}(\mathbf{k}) C_{\mu\nu, k\alpha}, \quad (\text{A2})$$

given by Eqs. (12) and (14), respectively, where

$$\varphi_{\mu, k\alpha}(t) = \sum_n e^{in\omega t} C_{\mu n, k\alpha}. \quad (\text{A3})$$

There are the unitarity relations regarding the matrix $\{C_{\mu\nu, \alpha'}\}$, given by

$$\sum_{\mu\nu} C_{\mu\nu, k\alpha}^* C_{\mu\nu, k\alpha'} = \delta_{\alpha\alpha'} \quad (\text{A4})$$

and

$$\sum_{\alpha} C_{\nu n, k\alpha} C_{\mu n', k\alpha}^* = \delta_{\mu\nu} \delta_{nn'}. \quad (\text{A5})$$

Here, the orthonormalization relation for $\varphi_{\nu, k\alpha}(t)$ is given by

$$\frac{1}{T} \int_0^T dt \sum_{\mu} \varphi_{\mu, k\alpha}^*(t) \varphi_{\mu, k\alpha'}(t) = \delta_{\alpha\alpha'} \quad (\text{A6})$$

and the associated closure relation is given by

$$\frac{1}{N_{ph}} \sum_{\alpha} \varphi_{\nu, k\alpha}(t) \varphi_{\mu, k\alpha}^*(t) = \delta_{\nu\mu}, \quad (\text{A7})$$

where $N_{ph} = \sum_{N_{\alpha}} 1$. This is readily verified as follows:

$$\begin{aligned} \frac{1}{N_{ph}} \sum_{\alpha} \varphi_{\nu, k\alpha}(t) \varphi_{\mu, k\alpha}^*(t) &= \frac{1}{N_{ph}} \sum_{\alpha, n, n'} e^{i(n-n')\omega t} C_{\nu n, k\alpha} C_{\mu n', k\alpha}^* \\ &= \frac{1}{N_{ph}} \sum_{n, N} e^{iN\omega t} \delta_{\nu\mu} \delta_{N0} \\ &= \delta_{\nu\mu} \frac{1}{N_{ph}} \sum_n 1 = \delta_{\nu\mu}. \end{aligned} \quad (\text{A8})$$

Further, it is shown that Eq. (A1) becomes

$$\begin{aligned} \sum_{\nu} L_{F\mu\nu}(\mathbf{k}, t) [e^{iN\omega t} \varphi_{\nu, k\alpha}(t)] &= [E_{\alpha}(\mathbf{k}) + N\omega] [e^{iN\omega t} \varphi_{\mu, k\alpha}(t)] \\ &= E_{\alpha(N)}(\mathbf{k}) [e^{iN\omega t} \varphi_{\mu, k\alpha}(t)], \end{aligned} \quad (\text{A9})$$

with $E_{\alpha(N)}(\mathbf{k}) \equiv E_{\alpha}(\mathbf{k}) + N\omega$, and thus one obtains the relation that

$$e^{iN\omega t} \varphi_{\nu, k\alpha}(t) = \varphi_{\nu, k\alpha(N)}(t). \quad (\text{A10})$$

Here, it is understood that the photon sideband α is represented as $\alpha_0(N_{\alpha})$, where $\alpha_0[\equiv \alpha_0(0)]$ and N_{α} stand for a parent band and the number of the sideband, respectively. Further, $\alpha(N) \equiv \alpha_0(N_{\alpha} + N)$ and $E_{\alpha(N)}(\mathbf{k}) = E_{\alpha_0}(\mathbf{k}) + (N_{\alpha} + N)\omega$. In view of Eq. (A3), Eq. (A10) is recast into

$$\begin{aligned} \varphi_{\nu, k\alpha}(t) &= \sum_n e^{in\omega t} C_{\nu n, k\alpha} = e^{-iN\omega t} \varphi_{\nu, k\alpha(N)}(t) \\ &= \sum_n e^{i(n-N)\omega t} C_{\nu n, k\alpha(N)} \\ &= \sum_{n'} e^{in'\omega t} C_{\nu(n'+N), k\alpha(N)}, \end{aligned} \quad (\text{A11})$$

leading to the relation that

$$C_{\nu n, k\alpha} = C_{\nu(n+N), k\alpha(N)}. \quad (\text{A12})$$

According to Eq. (23), given by

$$\hat{b}_{k\alpha}^{\dagger}(t) = \sum_{\mu} \hat{a}_{k\mu}^{\dagger}(t) \varphi_{\mu, k\alpha}(t) \theta(t), \quad (\text{A13})$$

the operator $\hat{b}_{k\alpha}^{\dagger}(t)$ pertinent to the creation of the Floquet quasiparticle is subject to the relation

$$e^{iN\omega t} \hat{b}_{k\alpha}^{\dagger}(t) = \hat{b}_{k\alpha(N)}^{\dagger}(t) \quad (\text{A14})$$

due to Eq. (A10). By employing Eqs. (A3) and (A5), Eq. (A13) is rewritten as

$$\begin{aligned} \sum_{\alpha} \hat{b}_{k\alpha}^{\dagger}(t) e^{-in\omega t} C_{v\alpha, k\alpha}^{*} &= \sum_{\alpha\mu} \hat{a}_{k\mu}^{\dagger}(t) e^{-in\omega t} \varphi_{\mu, k\alpha}(t) C_{v\alpha, k\alpha}^{*} \theta(t) \\ &= \sum_{\alpha\mu n'} \hat{a}_{k\mu}^{\dagger}(t) e^{i(-n+n')\omega t} C_{\mu n', k\alpha} C_{v\alpha, k\alpha}^{*} \theta(t) \\ &= \hat{a}_{k\nu}^{\dagger}(t). \end{aligned} \quad (\text{A15})$$

Hence, in view of Eqs. (A14) and (A12), the inverse-transformed relation from Eq. (A13) is obtained as

$$\begin{aligned} \hat{a}_{k\nu}^{\dagger}(t) &= \sum_{\alpha(-n)} \hat{b}_{k\alpha(-n)}^{\dagger}(t) C_{v0, k\alpha(-n)}^{*} \\ &= \sum_{\alpha} \hat{b}_{k\alpha}^{\dagger}(t) C_{v0, k\alpha}^{*}. \end{aligned} \quad (\text{A16})$$

Here, the matrix element $H_{F\lambda\mu}(\mathbf{k}, t)$ is rewritten in terms of the Floquet eigenstates. One begins with Eq. (A1) of the form

$$\sum_{\nu} H_{F\lambda\nu}(\mathbf{k}, t) \varphi_{\nu, k\alpha}(t) = \varphi_{\lambda, k\alpha}(t) E_{\alpha}(\mathbf{k}) + i \frac{d\varphi_{\lambda, k\alpha}(t)}{dt}. \quad (\text{A17})$$

Multiplying the left-hand side of this by $\varphi_{\mu, k\alpha}^{*}(t)$, followed by taking the summation over α , leads to

$$\frac{1}{N_{ph}} \sum_{\nu\alpha} H_{F\lambda\nu}(\mathbf{k}, t) \varphi_{\nu, k\alpha}(t) \varphi_{\mu, k\alpha}^{*}(t) = H_{F\lambda\mu}(\mathbf{k}, t), \quad (\text{A18})$$

where Eq. (A7) is employed. On the other hand, the right-hand side of Eq. (A17) becomes

$$\begin{aligned} &\frac{1}{N_{ph}} \sum_{\alpha} \left(\varphi_{\lambda, k\alpha}(t) E_{\alpha}(\mathbf{k}) \varphi_{\mu\alpha}^{*}(t) + i \frac{d\varphi_{\lambda, k\alpha}(t)}{dt} \varphi_{\mu, k\alpha}^{*}(t) \right) \\ &= \frac{1}{N_{ph}} \sum_{\alpha, n, n'} e^{i(n-n')\omega t} [E_{\alpha}(\mathbf{k}) - n\omega] C_{\lambda n, k\alpha} C_{\mu n', k\alpha}^{*} \\ &= \frac{1}{N_{ph}} \sum_{\alpha, n, N} e^{-iN\omega t} E_{\alpha(-n)}(\mathbf{k}) C_{\lambda 0, k\alpha(-n)} C_{\mu N, k\alpha(-n)}^{*} \\ &= \frac{1}{N_{ph}} \sum_{\alpha, n} E_{\alpha(-n)}(\mathbf{k}) C_{\lambda 0, k\alpha(-n)} \varphi_{\mu, k\alpha(-n)}^{*}(t) \\ &= \frac{1}{N_{ph}} \sum_n \sum_{\alpha} E_{\alpha}(\mathbf{k}) C_{\lambda 0, k\alpha} \varphi_{\mu, k\alpha}^{*}(t) \\ &= \sum_{\alpha} E_{\alpha}(\mathbf{k}) C_{\lambda 0, k\alpha} \varphi_{\mu, k\alpha}^{*}(t), \end{aligned} \quad (\text{A19})$$

where Eqs. (A3) and (A12) are employed. Thus one obtains

$$H_{F\lambda\mu}(\mathbf{k}, t) = \sum_{\alpha} E_{\alpha}(\mathbf{k}) C_{\lambda 0, k\alpha} \varphi_{\mu, k\alpha}^{*}(t) \quad (\text{A20})$$

and this is also rewritten as

$$\begin{aligned} H_{F\lambda\mu}(\mathbf{k}, t) &= H_{F\lambda\mu}^{*}(\mathbf{k}, t) \\ &= \sum_{\alpha} E_{\alpha}(\mathbf{k}) C_{\mu 0, k\alpha}^{*} \varphi_{\lambda, k\alpha}(t). \end{aligned} \quad (\text{A21})$$

Finally, the following relation is noted as

$$I_{\mu}(-1)^n C_{\mu n, k\alpha} = C_{\mu n, -k\alpha} \tilde{I}_{k\alpha}, \quad (\text{A22})$$

where I_{μ} and $\tilde{I}_{k\alpha}$ represent the parity of band μ and a constant phase factor with $|\tilde{I}_{k\alpha}| = 1$, respectively. For more detail, consult the Supplemental Material [91]. In particular, $\tilde{I}_{k\alpha}$ plays a role of the parity of the time-glide spatial inversion [44,45] at $\mathbf{k} = \mathbf{k}_0$, where \mathbf{k}_0 represents a high-symmetry momentum equal to $\mathbf{G}/2$ with \mathbf{G} a reciprocal lattice vector satisfying $\mathbf{G} \cdot \mathbf{R} = 2n\pi$ with n an integer.

APPENDIX B: DERIVATION OF EQ. (73)

Equation (69) is rewritten in the Bloch representation, where the Wannier state $|\mu\mathbf{R}\rangle$ is represented in terms of the Bloch state $|\mu\mathbf{k}\rangle$ as

$$|\mu\mathbf{R}\rangle = \frac{1}{\sqrt{N}} \sum_{\mathbf{k}} e^{-i\mathbf{k}\cdot\mathbf{R}} |\mu\mathbf{k}\rangle, \quad (\text{B1})$$

with \mathbf{k} as the Bloch momentum and N the number of the sites. In light of the fact that Eq. (69) is expressed as

$$\begin{aligned} &\sum_{\mu_1 \mathbf{R}_1 \mu_2 \mathbf{R}_2 \mu' \mathbf{k}'} \langle \mu\mathbf{k} | \mu_1 \mathbf{R}_1 \rangle e^{-i\mathbf{A}(t)\cdot\mathbf{R}_1} \tilde{h}_{\mu_1 \mathbf{R}_1, \mu_2 \mathbf{R}_2}(t) e^{i\mathbf{A}(t)\cdot\mathbf{R}_2} \\ &\times \langle \mu_2 \mathbf{R}_2 | \mu' \mathbf{k}' \rangle \langle \mu' \mathbf{k}' | \hat{\Phi} \rangle = i \frac{\partial}{\partial t} \langle \mu\mathbf{k} | \hat{\Phi} \rangle, \end{aligned} \quad (\text{B2})$$

one obtains the following equation as

$$\sum_{\mu' \mathbf{k}'} \langle \mu\mathbf{K}(t) | \tilde{h}(t) | \mu' \mathbf{K}'(t) \rangle \hat{\Phi}_{\mu' \mathbf{k}'} = i \frac{\partial}{\partial t} \hat{\Phi}_{\mu\mathbf{k}}, \quad (\text{B3})$$

with $\mathbf{K}(t) \equiv \mathbf{k} + \mathbf{A}(t)$, $\mathbf{K}'(t) \equiv \mathbf{k}' + \mathbf{A}(t)$, and $\hat{\Phi}_{\mu\mathbf{k}} \equiv \langle \mu\mathbf{k} | \hat{\Phi} \rangle$, where, in view of Eq. (B1), the relations of

$$\sum_{\mu_1 \mathbf{R}_1} \langle \mu\mathbf{k} | \mu_1 \mathbf{R}_1 \rangle \langle \mu_1 \mathbf{R}_1 | e^{-i\mathbf{A}(t)\cdot\mathbf{R}_1} = \langle \mu\mathbf{K}(t) | \quad (\text{B4})$$

and

$$\sum_{\mu_2 \mathbf{R}_2} e^{i\mathbf{A}(t)\cdot\mathbf{R}_2} |\mu_2 \mathbf{R}_2\rangle \langle \mu_2 \mathbf{R}_2 | \mu' \mathbf{k}' \rangle = |\mu' \mathbf{K}'(t)\rangle \quad (\text{B5})$$

are employed. Furthermore, the Hamiltonian matrix element of Eq. (B3) becomes

$$\begin{aligned} &\langle \mu\mathbf{K}(t) | \tilde{h}(t) | \mu' \mathbf{K}'(t) \rangle \\ &= \int d\mathbf{r} \int d\mathbf{r}' e^{-i\mathbf{K}\cdot\mathbf{r}} U_{\mu\mathbf{K}(t)}^{*}(\mathbf{r}) \tilde{h}(\mathbf{r}, \mathbf{r}'; t) e^{i\mathbf{K}'\cdot\mathbf{r}'} U_{\mu' \mathbf{K}'(t)}(\mathbf{r}') \\ &\approx \langle U_{\mu 0}(\mathbf{r}) | e^{-i\mathbf{K}(t)\cdot\mathbf{r}} h^0(\mathbf{r}) e^{i\mathbf{K}(t)\cdot\mathbf{r}} | U_{\mu' 0}(\mathbf{r}) \rangle \delta_{\mathbf{k}\mathbf{k}'} \\ &\quad + \int d\mathbf{r} \int d\mathbf{r}' e^{-i\mathbf{K}\cdot\mathbf{r}} U_{\mu 0}^{*}(\mathbf{r}) \mathbf{F}(t) \cdot \chi(\mathbf{r}, \mathbf{r}') e^{i\mathbf{K}'\cdot\mathbf{r}'} U_{\mu' 0}(\mathbf{r}') \\ &= \langle \chi_{\mu}(\mathbf{r}) | e^{-i\mathbf{K}(t)\cdot\mathbf{r}} h(\mathbf{r}, t) e^{i\mathbf{K}(t)\cdot\mathbf{r}} | \chi_{\mu'}(\mathbf{r}) \rangle \delta_{\mathbf{k}\mathbf{k}'}. \end{aligned} \quad (\text{B6})$$

In the first equality, Eq. (71) is employed and the periodic part of the Bloch wave function $\langle \mathbf{r} | \mu\mathbf{K}(t) \rangle$ is represented as $U_{\mu\mathbf{K}(t)}(\mathbf{r})$. In the last two equalities, this is replaced by

$$U_{\mu 0}(\mathbf{r}) = \frac{1}{\sqrt{N}} \sum_{\mathbf{R}} \chi_{\mu}(\mathbf{r} - \mathbf{R}), \quad (\text{B7})$$

following the conventional recipe of the $\mathbf{k} \cdot \mathbf{p}$ perturbation theory, where a Wannier function is introduced as $\chi_\mu(\mathbf{r}) = \langle \mathbf{r} | \mu \rangle$ and $\langle \mathbf{r} | \mu \mathbf{R} \rangle$ is represented as $\langle \mathbf{r} | \mu \mathbf{R} \rangle = \langle \mathbf{r} - \mathbf{R} | \chi_\mu \rangle = \chi_\mu(\mathbf{r} - \mathbf{R})$. The resulting expression is in agreement with $H_{\mu\mu'}(\mathbf{k}, t) \delta_{\mathbf{k}\mathbf{k}'}$ of Eq. (20). By comparing Eq. (B3) with Eq. (20), one comes to the conclusion that $\hat{\Phi}_{\mu\mathbf{k}}(t) = \hat{a}_{\mathbf{k}\mu}(t)$ given in Eq. (73).

APPENDIX C: EXPRESSIONS FOR THE SURFACE MAGNETIZATION

Equations (81) and (82) are rewritten to conform to the surface magnetization. First, the operator $\hat{a}_{\mathbf{k}\mu}(t)$ of Eq. (73) is read as

$$\begin{aligned} \hat{a}_{\mathbf{k}\mu}(t) &= \langle \mu \mathbf{k} | \hat{\Phi}(t) \rangle \\ &= \sum_{\bar{\mathbf{k}}'_{R_y}} \langle \mu \mathbf{k} | \mu \bar{\mathbf{k}}'_{R_y} \rangle \langle \mu \bar{\mathbf{k}}'_{R_y} | \hat{\Phi}(t) \rangle \\ &= \frac{1}{\sqrt{N_y}} \sum_{R_y} e^{-i\mathbf{k}_y R_y} \hat{\alpha}_{\bar{\mathbf{k}}_{R_y, \mu}}(t), \end{aligned} \quad (\text{C1})$$

with N_y the number of sites in the y direction, where an alternative operator in the partial site representation $\hat{\alpha}_{\bar{\mathbf{k}}_{R_y, \mu}}(t)$ is defined as $\langle \mu \bar{\mathbf{k}}_{R_y} | \hat{\Phi}(t) \rangle$. Thus the density matrix of Eq. (21) is recast into

$$\rho_{\mathbf{k}\mu\nu}(t) = \frac{1}{N_y} \sum_{R_y, \Delta R_y} e^{-i\mathbf{k}_y \Delta R_y} \langle \hat{\alpha}_{\bar{\mathbf{k}}_{R_y, \mu}}^\dagger(t) \hat{\alpha}_{\bar{\mathbf{k}}_{(R_y - \Delta R_y), \nu}}(t) \rangle_g. \quad (\text{C2})$$

The spatial average density matrix in the bulk is given by

$$\eta_{\mu\nu}^{(b)}(t) = \frac{1}{V} \sum_{\mathbf{k}} \rho_{\mathbf{k}\mu\nu}(t) = \frac{1}{V} \sum_{\bar{\mathbf{k}}_{R_y}} \rho'_{\bar{\mathbf{k}}_{R_y, \mu\nu}}(t), \quad (\text{C3})$$

where

$$\rho'_{\bar{\mathbf{k}}_{R_y, \mu\nu}}(t) = \langle \hat{\alpha}_{\bar{\mathbf{k}}_{R_y, \mu}}^\dagger(t) \hat{\alpha}_{\bar{\mathbf{k}}_{R_y, \nu}}(t) \rangle_g, \quad (\text{C4})$$

and the summation over \mathbf{k} is taken in the whole BZ in the first equality. On the other hand, it is necessary to evaluate the corresponding density matrix in the surface, defined as

$$\eta_{\mu\nu}^{(s)}(t) = \frac{1}{S_{xz}} \sum_{\bar{\mathbf{k}}} (\rho'_{\bar{\mathbf{k}}_{0, \mu\nu}}(t) + \rho'_{\bar{\mathbf{k}}_{L_y, \mu\nu}}(t)), \quad (\text{C5})$$

with S_{xz} a surface area in the $x - z$ plane, where the summation over $\bar{\mathbf{k}}$ is taken in the limited area of the two-dimensional

BZ where surface states are present. Just both outermost sites in the y direction, namely, $R_y = 0$ and L_y , are taken in the density matrix of Eq. (C4); L_y represents the size of the crystal in the y direction. It is remarked that $\rho'_{\bar{\mathbf{k}}_{R_y, \mu\nu}}(t)$ is given by converting Eqs. (35)–(39) to the corresponding expressions in the partial-site representation.

Eventually, the surface magnetization is provided by

$$\bar{\mathbf{M}}^{(\text{sol})}(t) \approx \mu_B \text{Re} \sum_{\mu\nu} \eta_{\mu\nu}^{(s)}(t) \langle \mu | g_e \mathbf{s} + \mathbf{l} + \mathbf{r} \times \mathbf{A}(t) | \nu \rangle. \quad (\text{C6})$$

Hence it is found that this arises from the spin magnetization ($g_e \mathbf{s}$), the orbital magnetization (\mathbf{l}) relevant to the IFE, and the remaining term [$\mathbf{r} \times \mathbf{A}(t)$] due to the gauge correction. Here, it is noted that the term $\sum_{\mathbf{k}} \rho_{\mathbf{k}\mu\nu}(t) \langle \mu | \mathbf{r} | \nu \rangle \times \mathbf{k}$, which is seen in Eq. (82), is neglected. This is because the leading contribution of the polarization coherence $f(t) \equiv \rho_{\mathbf{k}\mu\nu}(t)$ with $\mu \neq \nu$ arises from the linear optical process with respect to the laser field $\mathbf{F}(t)$, and most of the dipole transitions are effective only when the almost on-resonant condition of $\omega \approx E_g \approx \Delta_{\mu\nu}(\mathbf{k})$ is met, namely, in the vicinity of the Γ point, where $\Delta_{\mu\nu}(\mathbf{k})$ represents the energy difference between bands μ and ν . This statement leads to the assumption that the associated induced magnetization vanishes in the asymptotic limit of time.

Below, this is verified in more detail. The procedure of taking the infinite limit of t on the nonsingular function $f(t)$ in the interval $[0, \infty)$ is replaced by another procedure of taking a limit of an infinitesimal value of ϵ , which is given by

$$\lim_{t \rightarrow \infty} f(t) = \lim_{\epsilon \rightarrow +0} \epsilon \int_0^\infty dt e^{-\epsilon t} f(t). \quad (\text{C7})$$

This equality is simply verified by taking a partial differentiation with respect to t in the right-hand side. Given

$$f(t) = \sum_n e^{i\omega_n t} f_n, \quad (\text{C8})$$

with $\omega_n \neq 0$ for $n \neq 0$ and $\omega_0 = 0$, it is shown that

$$\lim_{t \rightarrow \infty} f(t) = \lim_{\epsilon \rightarrow +0} \sum_n f_n \frac{\epsilon}{\epsilon - i\omega_n} = f_0, \quad (\text{C9})$$

implying that all of the oscillating terms of $f(t)$ vanish asymptotically and just a constant contribution f_0 is extracted. Since the leading term of $f(t)$ is linear in $\mathbf{F}(t)$, as stated above, f_0 is considered to almost vanish. Besides, it is remarked that there would possibly remain small nonzero contributions due to higher-order optical processes just in the vicinity of $\mathbf{k} = \mathbf{0}$. Therefore, it is concluded that $\sum_{\mathbf{k}} \rho_{\mathbf{k}\mu\nu}(t) \langle \mu | \mathbf{r} | \nu \rangle \times \mathbf{k} \approx \mathbf{0}$ in Eq. (82).

- [1] S. Murakami, S. Iso, Y. Avishai, M. Onoda, and N. Nagaosa, Tuning phase transition between quantum spin Hall and ordinary insulating phases, *Phys. Rev. B* **76**, 205304 (2007).
- [2] S. Murakami, Phase transition between the quantum spin Hall and insulator phases in 3D: Emergence of a topological gapless phase, *New J. Phys.* **9**, 356 (2007); **10**, 029802 (2008).
- [3] Z. Wang, Y. Sun, X.-Q. Chen, C. Franchini, G. Xu, H. Weng, X. Dai, and Z. Fang, Dirac semimetal and topological phase

transitions in $A_3\text{Bi}$ ($A = \text{Na, K, Rb}$), *Phys. Rev. B* **85**, 195320 (2012).

- [4] Z. Wang, H. Weng, Q. Wu, X. Dai, and Z. Fang, Three-dimensional Dirac semimetal and quantum transport in Cd_3As_2 , *Phys. Rev. B* **88**, 125427 (2013).
- [5] S. M. Young, S. Zaheer, J. C. Y. Teo, C. L. Kane, E. J. Mele, and A. M. Rappe, Dirac semimetal in three dimensions, *Phys. Rev. Lett.* **108**, 140405 (2012).
- [6] S. M. Young and C. L. Kane, Dirac semimetals in two dimensions, *Phys. Rev. Lett.* **115**, 126803 (2015).

- [7] B.-J. Yang and N. Nagaosa, Classification of stable three-dimensional Dirac semimetals with nontrivial topology, *Nat. Commun.* **5**, 4898 (2014).
- [8] H. Yi, Z. Wang, C. Chen, Y. Shi, Y. Feng, A. Liang, Z. Xie, S. He, J. He, Y. Peng, X. Liu, Y. Liu, L. Zhao, G. Liu, X. Dong, J. Zhang, M. Nakatake, M. Arita, K. Shimada, H. Namatame *et al.*, Evidence of topological surface state in three-dimensional Dirac semimetal Cd_3As_2 , *Sci. Rep.* **4**, 6106 (2014).
- [9] S.-Y. Xu, I. Belopolski, N. Alidoust, M. Neupane, G. Bian, C. Zhang, R. Sankar, G. Chang, Z. Yuan, C.-C. Lee, S.-M. Huang, H. Zheng, J. Ma, D. S. Sanchez, B. Wang, A. Bansil, F. Chou, P. P. Shibayev, H. Lin, S. Jia *et al.*, Discovery of a Weyl fermion semimetal and topological Fermi arcs, *Science* **349**, 613 (2015).
- [10] M. Kargariana, M. Randeria, and Y.-M. Lu, Are the surface Fermi arcs in Dirac semimetals topologically protected? *Proc. Natl. Acad. Sci. USA* **113**, 8648 (2016).
- [11] S. Park and B.-J. Yang, Classification of accidental band crossings and emergent semimetals in two-dimensional noncentrosymmetric systems, *Phys. Rev. B* **96**, 125127 (2017).
- [12] H. Doh and H. J. Choi, Dirac-semimetal phase diagram of two-dimensional black phosphorus, *2D Mater.* **4**, 025071 (2017).
- [13] B. Yan and C. Felser, Topological materials: Weyl semimetals, *Annu. Rev. Condens. Matter Phys.* **8**, 337 (2017).
- [14] N. P. Armitage, E. J. Mele, and A. Vishwanath, Weyl and Dirac semimetals in three-dimensional solids, *Rev. Mod. Phys.* **90**, 015001 (2018).
- [15] S.-Y. Yang, H. Yang, E. Derunova, S. S. P. Parkin, B. Yan, and M. N. Ali, Symmetry demanded topological nodal-line materials, *Adv. Phys.* **X 3**, 1414631 (2018).
- [16] H. Weyl, Elektron und gravitation. I, *Z. Phys.* **56**, 330 (1929); Gravitation and the electron, *Proc. Natl. Acad. Sci. USA* **15**, 323 (1929).
- [17] E. Majorana, Teoria simmetrica dell'elettrone e del positrone, *Nuovo Cim.* **14**, 171 (1937).
- [18] S. R. Elliott and M. Franz, Colloquium: Majorana fermions in nuclear, particle, and solid-state physics, *Rev. Mod. Phys.* **87**, 137 (2015).
- [19] S. L. Adler, Axial-vector vertex in synor electrodynamics, *Phys. Rev.* **177**, 2426 (1969).
- [20] J. S. Bell and R. Jackiw, A PCAC puzzle: $\pi^0 \rightarrow \gamma\gamma$ in the σ -model, *Nuovo Cim. A* **60**, 47 (1969).
- [21] H. B. Nielsen and M. Ninomiya, The Adler-Bell-Jackiw anomaly and Weyl fermions in a crystal, *Phys. Lett. B* **130**, 389 (1983).
- [22] C. Shekhar, A. K. Nayak, Y. Sun, M. Schmidt, M. Nicklas, I. Leermakers, U. Zeitler, Y. Skourski, J. Wosnitza, Z. Liu, and Y. Chen, Extremely large magnetoresistance and ultrahigh mobility in the topological Weyl semimetal candidate NbP, *Nat. Phys.* **11**, 645 (2015).
- [23] A. Gynther, K. Landsteiner, F. Pena-Benitez, and A. Rebhan, Holographic anomalous conductivities and the chiral magnetic effect, *J. High Energy Phys.* **02** (2011) 110.
- [24] D. T. Son and B. Z. Spivak, Chiral anomaly and classical negative magnetoresistance of Weyl metals, *Phys. Rev. B* **88**, 104412 (2013).
- [25] F. Arnold, C. Shekhar, S.-C. Wu, Y. Sun, R. D. Dos Reis, N. Kumar, M. Naumann, M. O. Ajeesh, M. Schmidt, A. G. Grushin, and J. H. Bardarson, Negative magnetoresistance without well-defined chirality in the Weyl semimetal TaP, *Nat. Commun.* **7**, 11615 (2016).
- [26] X. Huang, L. Zhao, Y. Long, P. Wang, D. Chen, Z. Yang, H. Liang, M. Xue, H. Weng, Z. Fang, and X. Dai, Observation of the chiral-anomaly-induced negative magnetoresistance in 3D Weyl semimetal TaAs, *Phys. Rev. X* **5**, 031023 (2015).
- [27] M. Ali, J. Xiong, S. Flynn, J. Tao, Q. Gibson, L. Schoop, T. Liang, N. Haldolaarachchige, M. Hirschberger, N. Ong, and R. Cava, Large, non-saturating magnetoresistance in WTe_2 , *Nature (London)* **514**, 205 (2014).
- [28] A. A. Burkov, Chiral anomaly and diffusive magnetotransport in Weyl metals, *Phys. Rev. Lett.* **113**, 247203 (2014).
- [29] A. A. Burkov, Chiral anomaly and transport in Weyl metals, *J. Phys.: Condens. Matter* **27**, 113201 (2015).
- [30] J. Xiong, S. K. Kushwaha, T. Liang, J. W. Krizan, M. Hirschberger, W. Wang, R. J. Cava, and N. P. Ong, Evidence for the chiral anomaly in the Dirac semimetal Na_3Bi , *Science* **350**, 413 (2015).
- [31] C.-L. Zhang, S.-Y. Xu, I. Belopolski, Z. Yuan, Z. Lin, B. Tong, G. Bian, N. Alidoust, C.-C. Lee, S.-M. Huang, T.-R. Chang, G. Chang, C.-H. Hsu, H.-T. Jeng, M. Neupane, D. S. Sanchez, H. Zheng, J. Wang, H. Lin, C. Zhang *et al.*, Signatures of the Adler-Bell-Jackiw chiral anomaly in a Weyl fermion semimetal, *Nat. Commun.* **7**, 10735 (2016).
- [32] R. Wang, B. Wang, R. Shen, L. Sheng, D. Y. Xing, and S. Y. Savrasov, Floquet Weyl semimetal induced by off-resonant light, *Europhys. Lett.* **105**, 17004 (2014).
- [33] K. Taguchi, T. Imaeda, M. Sato, and Y. Tanaka, Photovoltaic chiral magnetic effect in Weyl semimetals, *Phys. Rev. B* **93**, 201202(R) (2016).
- [34] K. Taguchi, D.-H. Xu, A. Yamakage, and K. T. Law, Photovoltaic anomalous Hall effect in line-node semimetals, *Phys. Rev. B* **94**, 155206 (2016).
- [35] H. Hübener, M. A. Sentef, U. De Giovannini, A. F. Kemper, and A. Rubio, Creating stable Floquet-Weyl semimetals by laser-driving of 3D Dirac materials, *Nat. Commun.* **8**, 13940 (2016).
- [36] J.-Y. Zou and B.-G. Liu, Floquet Weyl fermions in three-dimensional stacked graphene systems irradiated by circularly polarized light, *Phys. Rev. B* **93**, 205435 (2016).
- [37] X.-X. Zhang, T. T. Ong, and N. Nagaosa, Theory of photoinduced Floquet Weyl semimetal phases, *Phys. Rev. B* **94**, 235137 (2016).
- [38] Z. Yan and Z. Wang, Tunable Weyl points in periodically driven nodal line semimetals, *Phys. Rev. Lett.* **117**, 087402 (2016).
- [39] Z. Yan and Z. Wang, Floquet multi-Weyl points in crossing-nodal-line semimetals, *Phys. Rev. B* **96**, 041206(R) (2017).
- [40] N. Goldman and J. Dalibard, Periodically driven quantum systems: Effective Hamiltonians and engineered gauge fields, *Phys. Rev. X* **4**, 031027 (2014).
- [41] K. Plekhanov, G. Roux, and K. Le Hur, Floquet engineering of Haldane Chern insulators and chiral bosonic phase transitions, *Phys. Rev. B* **95**, 045102 (2017).
- [42] T. Oka and S. Kitamura, Floquet engineering of quantum materials, *Annu. Rev. CMP* **10**, 387 (2019).
- [43] M. S. Rudner and N. H. Lindner, Band structure engineering and non-equilibrium dynamics in Floquet topological insulators, *Nat. Rev. Phys.* **2**, 229 (2020).
- [44] B. Zhang, N. Maeshima, and K. Hino, Edge states of Floquet-Dirac semimetal in a laser-driven semiconductor quantum-well, *Sci. Rep.* **11**, 2952 (2021).

- [45] T. Morimoto, H. C. Po, and A. Vishwanath, Floquet topological phases protected by time glide symmetry, *Phys. Rev. B* **95**, 195155 (2017).
- [46] R. Chen, B. Zhou, and D.-H. Xu, Floquet Weyl semimetals in light-irradiated type-II and hybrid line-node semimetals, *Phys. Rev. B* **97**, 155152 (2018); **100**, 049901(E) (2019).
- [47] U. Kumar, Anisotropic Floquet optical spectra of Weyl semimetal, *Mater. Res. Express* **6**, 096304 (2019).
- [48] Y. Zhu, T. Qin, X. Yang, G. Xianlong, and Z. Liang, Floquet and anomalous Floquet Weyl semimetals, *Phys. Rev. Res.* **2**, 033045 (2020).
- [49] G. Salerno, N. Goldman, and G. Palumbo, Floquet-engineering of nodal rings and nodal spheres and their characterization using the quantum metric, *Phys. Rev. Res.* **2**, 013224 (2020).
- [50] Y. Gao, C. Wang, and D. Xiao, Topological inverse Faraday effect in Weyl semimetals, [arXiv:2009.13392](https://arxiv.org/abs/2009.13392) [cond-mat.mes-hall].
- [51] I. D. Tokman, Q. Chen, I. A. Shereshevsky, V. I. Pozdnyakova, I. Oladyshekin, M. Tokman, and A. Belyanin, Inverse Faraday effect in graphene and Weyl semimetals, *Phys. Rev. B* **101**, 174429 (2020).
- [52] M. Kawaguchi, H. Hirose, Z. Chi, Y.-C. Lau, F. Freimuth, and M. Hayashi, Giant inverse Faraday effect in Dirac semimetals, [arXiv:2009.01388](https://arxiv.org/abs/2009.01388) [cond-mat.mes-hall].
- [53] L. Liang, P. O. Sukhachov, and A. V. Balatsky, Axial magnetoelectric effect in Dirac semimetals, *Phys. Rev. Lett.* **126**, 247202 (2021).
- [54] J. Ma and D. A. Pesin, Chiral magnetic effect and natural optical activity in metals with or without Weyl points, *Phys. Rev. B* **92**, 235205 (2015).
- [55] F. de Juan, A. G. Grushin, T. Morimoto, and J. E. Moore, Quantized circular photogalvanic effect in Weyl semimetals, *Nat. Commun.* **8**, 15995 (2017).
- [56] S. A. A. Ghorashi, P. Hosur, and C.-S. Ting, Irradiated three-dimensional Luttinger semimetal: A factory for engineering Weyl semimetals, *Phys. Rev. B* **97**, 205402 (2018).
- [57] M. Umer, R. W. Bomantara, and J. Gong, Nonequilibrium hybrid multi-Weyl semimetal phases, *J. Phys. Mater.* **4**, 045003 (2021).
- [58] M. Umer, R. W. Bomantara, and J. Gong, Dynamical characterization of Weyl nodes in Floquet Weyl semimetal phases, *Phys. Rev. B* **103**, 094309 (2021).
- [59] R. Zhang, K. Hino, and N. Maeshima, Floquet-Weyl semimetals generated by an optically resonant interband transition, *Phys. Rev. B* **106**, 085206 (2022).
- [60] N. Yoshikawa, K. Ogawa, Y. Hirai, K. Fujiwara, J. Ikeda, A. Tsukazaki, and R. Shimano, Non-volatile chirality switching by all-optical magnetization reversal in ferromagnetic Weyl semimetal $\text{Co}_3\text{Sn}_2\text{S}_2$, *Commun. Phys.* **5**, 328 (2022).
- [61] C. Guo, V. S. Asadchy, B. Zhao, and S. Fan, Light control with Weyl semimetals, *eLight* **3**, 2 (2023).
- [62] M. Hasan, D. Yudin, I. Iorsh, O. Eriksson, and I. Shelykh, Topological edge-state engineering with high-frequency electromagnetic radiation, *Phys. Rev. B* **96**, 205127 (2017).
- [63] F. Casas, J. A. Oteo, and J. Ros, Floquet theory: Exponential perturbative treatment, *J. Phys. A: Math. Gen.* **34**, 3379 (2001).
- [64] E. S. Mananga and T. Charpentier, Introduction of the Floquet-Magnus expansion in solid-state nuclear magnetic resonance spectroscopy, *J. Chem. Phys.* **135**, 044109 (2011).
- [65] A. Eckardt and E. Anisimovas, High-frequency approximation for periodically driven quantum systems from a Floquet-space perspective, *New J. Phys.* **17**, 093039 (2015).
- [66] E. S. Mananga and T. Charpentier, On the Floquet-Magnus expansion: Applications in solid-state nuclear magnetic resonance and physics, *Phys. Rep.* **609**, 1 (2016).
- [67] T. Haga, Divergence of the Floquet-Magnus expansion in a periodically driven one-body system with energy localization, *Phys. Rev. E* **100**, 062138 (2019).
- [68] P. S. Pershan, J. P. van der Ziel, and L. D. Malmstrom, Theoretical discussion of the inverse Faraday effect, Raman scattering, and related phenomena, *Phys. Rev.* **143**, 574 (1966).
- [69] A. V. Kimel, A. Kirilyuk, P. A. Usachev, V. Pisarev, A. M. Balbashov, and Th. Rasing, Ultrafast non-thermal control of magnetization by instantaneous photomagnetic pulses, *Nature (London)* **435**, 655 (2005).
- [70] K. Vahaplar, A. M. Kalashnikova, A. V. Kimel, D. Hinzke, U. Nowak, R. Chantrell, A. Tsukamoto, A. Itoh, A. Kirilyuk, and Th. Rasing, Ultrafast path for optical magnetization reversal via a strongly nonequilibrium state, *Phys. Rev. Lett.* **103**, 117201 (2009).
- [71] T. A. Ostler, J. Barker, R. F. L. Evans, R. W. Chantrell, U. Atxitia, O. Chubykalo-Fesenko, S. El Moussaoui, L. Le Guyader, E. Mengotti, L. J. Heyderman, F. Nolting, A. Tsukamoto, A. Itoh, D. Afanasiev, B. A. Ivanov, A. M. Kalashnikova, K. Vahaplar, J. Mentink, A. Kirilyuk, Th. Rasing, and A. V. Kimel, Ultrafast heating as a sufficient stimulus for magnetization reversal in a ferrimagnet, *Nat. Commun.* **3**, 666 (2012).
- [72] R. Hertel, Theory of the inverse Faraday effect in metals, *J. Magn. Magn. Mater.* **303**, L1 (2006).
- [73] H.-L. Zhang, Y.-Z. Wang, and X.-J. Chen, A simple explanation for the inverse Faraday effect in metals, *J. Magn. Magn. Mater.* **321**, L73 (2009).
- [74] S. R. Woodford, Conservation of angular momentum and the inverse Faraday effect, *Phys. Rev. B* **79**, 212412 (2009).
- [75] M. I. Kurkin, N. B. Bakulina, and R. V. Pisarev, Transient inverse Faraday effect and ultrafast optical switching of magnetization, *Phys. Rev. B* **78**, 134430 (2008).
- [76] K. Taguchi and G. Tatara, Theory of inverse Faraday effect in a disordered metal in the terahertz regime, *Phys. Rev. B* **84**, 174433 (2011).
- [77] D. Popova, A. Bringer, and S. Blügel, Theory of the inverse Faraday effect in view of ultrafast magnetization experiments, *Phys. Rev. B* **84**, 214421 (2011).
- [78] D. Popova, A. Bringer, and S. Blügel, Theoretical investigation of the inverse Faraday effect via a stimulated Raman scattering process, *Phys. Rev. B* **85**, 094419 (2012).
- [79] V. N. Gridnev, Optical spin pumping and magnetization switching in ferromagnets, *Phys. Rev. B* **88**, 014405 (2013).
- [80] A. Qaiumzadeh, G. E. W. Bauer, and A. Brataas, Manipulation of ferromagnets via the spin-selective optical Stark effect, *Phys. Rev. B* **88**, 064416 (2013).
- [81] M. Battiato, G. Barbalinardo, and P. M. Oppeneer, Quantum theory of the inverse Faraday effect, *Phys. Rev. B* **89**, 014413 (2014).
- [82] P. J. Lin-Chung, Energy-band structures of Cd_3As_2 and Zn_3As_2 , *Phys. Rev.* **188**, 1272 (1969).
- [83] K. Sierański, J. Szatkowski, and J. Misiewicz, Semiempirical tight-binding band structure of II_3V_2 semiconductors:

- Cd_3P_2 , Zn_3P_2 , Cd_3As_2 , and Zn_3As_2 , *Phys. Rev. B* **50**, 7331 (1994).
- [84] M. Neupane, S. Xu, R. Sankar, N. Alidoust, G. Bian, C. Liu, I. Belopolski, T. Chang, H. Jeng, H. Lin, A. Bansil, F. Chou, and M. Z. Hasan, Observation of a three-dimensional topological Dirac semimetal phase in high-mobility Cd_3As_2 , *Nat. Commun.* **5**, 3786 (2014).
- [85] Z. Liu, J. Jiang, B. Zhou, Z. Wang, Y. Zhang, H. Weng, D. Prabhakaran, S. Mo, H. Peng, P. Dudin, T. Kim, M. Hoesch, Z. Fang, X. Dai, Z. X. Shen, D. L. Feng, Z. Hussain, and Y. L. Chen, A stable three-dimensional topological Dirac semimetal Cd_3As_2 , *Nat. Mater.* **13**, 677 (2014).
- [86] I. Crassee, R. Sankar, W.-L. Lee, A. Akrap, and M. Orlita, 3D Dirac semimetal Cd_3As_2 : A review of material properties, *Phys. Rev. Mater.* **2**, 120302 (2018).
- [87] H. Okamoto, The As-Zn (Arsenic-Zinc) system, *J. Phase Equilib.* **13**, 155 (1992).
- [88] E. O. Kane, Band structure of indium antimonide, *J. Phys. Chem. Solids* **1**, 249 (1957).
- [89] J. M. Luttinger, Quantum theory of cyclotron resonance in semiconductors: General theory, *Phys. Rev.* **102**, 1030 (1956).
- [90] J. H. Shirley, Solution of the Schrödinger equation with a Hamiltonian periodic in time, *Phys. Rev.* **138**, B979 (1965).
- [91] See Supplemental Material at <http://link.aps.org/supplemental/10.1103/PhysRevB.108.155308> for Supplemental Note 1: Explicit expressions of density matrices of quasiparticle derived from the optical Bloch equations, and for Supplemental Note 2: Details of time-glide inversion symmetry and its associated parity eigenvalue, including the concomitant relation between eigenvectors of the Floquet eigenvalue equation at Bloch momenta with opposite directions.
- [92] Due to a heavy computational burden, the numerical calculations of the induced bulk magnetization are implemented just in the limited $k_x - k_z$ region, namely, $|k_x d_x|, |k_z d_z| \leq 0.1\pi$, in the bulk crystal that is confined in the y direction. The valence electrons with down spin are dominantly excited in the vicinity of the Γ point corresponding to the above region. The obtained result is about 0.4 mT at $t = 25T$, which is already almost constant in time. Thus, by simply extending the incorporated region of the $k_x - k_z$ plane from the above limited region to the whole region, the net bulk magnetization is estimated to be approximately $(\pi/0.1\pi)^2 \times 0.4 \text{ mT} = 40 \text{ mT}$, though this is merely an ideal maximum. This value is mostly ascribable to the IFE, not to both the spin magnetization and the gauge correction that are negligibly small.
- [93] J. Kerr, On rotation of the plane of polarization by reflection from the pole of a magnet, *Lond. Edinb. Dublin Philos. Mag. J. Sci.* **3**, 321 (1877).
- [94] P. Weinberger, John Kerr and his effects found in 1877 and 1878, *Philos. Mag. Lett.* **88**, 897 (2008).
- [95] T. Haider, A review of magneto-optic effects and its application, *Int. J. Electromagn. Appl.* **7**, 17 (2017).
- [96] M. Mehdi Jadidi, M. Kargarian, M. Mittendorff, Y. Aytac, B. Shen, J. C. König-Otto, S. Winnerl, N. Ni, A. L. Gaeta, T. E. Murphy, and H. Dennis Drew, Nonlinear optical control of chiral charge pumping in a topological Weyl semimetal, *Phys. Rev. B* **102**, 245123 (2020).
- [97] W. Schäfer and M. Wegener, *Semiconductor Optics and Transport Phenomena (Advanced Texts in Physics)* (Springer-Verlag, Heidelberg, Berlin, 2002), Chap. 10.